One-Bit Compressive Radar Sensing in the Presence of Clutter

SAYED JALAL ZAHABI, Member, IEEE
MOHAMMAD MAHDI NAGHSH, Member, IEEE
MAHMOUD MODARRES-HASHEMI
Isfahan University of Technology, Isfahan, Iran

JIAN LI, Fellow, IEEE
University of Florida, Gainesville, FL, USA

We propose a compressive pulse-Doppler radar that works through one-bit quantization of the received noisy signal by comparing it with a time-varying reference level. Considering the sparsity of the targets in the range-Doppler domain, we solve the problem by sparse recovery methods in both the absence and presence of clutter. The proposed method leads to an optimization problem that can be tackled by a convex approximation. Numerical examples confirm the effectiveness of the proposed method.

Manuscript received September 19, 2018; revised March 25, 2019; released for publication April 3, 2019. Date of publication May 20, 2019; date of current version February 7, 2020.

DOI. No. 10.1109/TAES.2019.2916532

Refereeing of this contribution was handled by P. Lombardo.

This work was supported in part by Iran National Science Foundation under Contract 94028968 and in part by the US National Science Foundation under Grant 1704240 and Grant 1708509.

Authors' addresses: S. J. Zahabi, M. M. Naghsh, and M. Modarres-Hashemi are with the Department of Electrical and Computer Engineering, Isfahan University of Technology, Isfahan 84156-83111, Iran, E-mail: (zahabi@cc.iut.ac.ir; mm_naghsh@cc.iut.ac.ir; modarres@cc.iut.ac.ir.); J. Li is with the Electrical and Computer Engineering Department, University of Florida, Gainesville, FL 32611 USA, E-mail: (li@dsp.ufl.edu). *(Corresponding author: Jian Li.)*

I. INTRODUCTION

Signal quantization is a key task in digital signal processing applications. The most ideal case of quantization in terms of signal amplitude resolution is to have infinite precision samples. In practice, however, the amplitude quantization precision (or equivalently the quantization bit-depth) is in tradeoff with the sampling rate, cost, and energy consumption.

From the bit-depth point of view, the most extreme form of quantization is to reduce the signal to one bit per sample, which can be performed simply by comparing the signal to a known reference level. This way, one-bit sampling is in fact to treat the quantized measurements as sign values instead of their true values. The main advantage of one-bit quantization is that it allows for very high sampling rates, at low cost and with low energy consumption. In some applications, the power consumption of one-bit sampling at a rate of 240 gigasamples/s is only about 10 mW, which is much less than the power that a conventional analog-to-digital converter (ADC) typically consumes [1], [2]. This is of great importance not only in portable battery-enabled technologies, but even in cases where a power supply exists, considering the *green communication* perspective. This energy efficiency is one of the motivating factors for using one-bit sampling in millimeter wave communications and massive multiple-input multiple-output communication/radar systems [4]. Moreover, the conventional ADC is rather expensive;[1] this is in contrast with the one-bit sampling, which is extremely inexpensive, allowing for a totally affordable system.

One-bit sampling has so far been studied in the literature from different perspectives. Some papers have looked into the topic in a classical statistical framework [5]–[9]. The topic has also been studied from a sampling/reconstruction viewpoint in works such as [10] and more recently in [11]. One-bit processing has also been used in radar signal coding in earlier works such as [12] and [13], and later in [14].

Most of the recent works on one-bit sampling, however, study the problem from a compressive sensing (CS) viewpoint [15]–[27]. It has been shown that sparse signals can be recovered with high accuracy from a sufficiently large record of one-bit measurements [18]. The early works in compressive one-bit sampling share a common limiting feature, which is considering a fixed quantization threshold (usually zero). Indeed, as argued in [25], with this limitation, it is not possible to determine the actual energy of the unknown signal. Some of the recent papers, in contrast, have considered random time-varying thresholds [25]–[27]. Specifically in [27], the problem of estimating signal parameters after quantization to single bit samples is considered where the one-bit samples are captured by comparing the signal to a time-varying reference level.

The authors of the present paper have recently proposed the idea of radar sensing via one-bit compressive sampling in [28] and [29]. In [28], it was shown that by quantizing the received noisy signal to one bit (using time-varying

[1]Conventional ADCs can typically cost thousands of dollars, even at sampling rates of 2 or 3 gigasamples/s [3].

thresholds), it is possible to perform the radar sensing for stationary targets. In [29], the case of radar sensing for moving targets (i.e., adding the Doppler effect to the scenario) was studied.

In this paper, we expand the problem in [29] to a more general and more practical framework, in which the clutter effect is taken into account as well. Specifically, we first propose a compressive pulse-Doppler radar that works in a clutter-free environment, through one-bit quantization of the received noisy signal, which is performed by comparing the signal with a time-varying threshold.[2] Since the targets are sparse in the range-Doppler domain, by using a sparse recovery method, the radar sensing objective is expressed as an optimization problem that can be tackled numerically. Then, we show how the sparse method can be modified in order to address the problem in the presence of clutter, and especially the case of strong clutter. The novelty of this paper is therefore, in 1) how the radar sensing problem in the general framework is formulated to employ a method of one-bit sparse estimation with time-varying thresholds and 2) how the method is generalized (and customized) to overcome the disturbing effects such as the strong clutter or the off-grid targets. Simulation results illustrate that the proposed method and its modified version have promising performance in the sensing of the targets, in both clutter-free and clutter-present environments. It is further seen that at low signal-to-noise ratio (SNR), increasing the sampling rate at the receiver compensates for the SNR, and hence improves the performance. Moreover, it is observed that in the case of multiple targets, increasing the sampling rate improves the sensing performance, from target resolution point of view.

The remainder of the paper is organized as follows. In Section II, we derive our model for the one-bit compressive pulse-Doppler radar and the relevant sensing problem is formulated. Then, we propose a solution, which employs a norm-based sparse framework. Then, in Section III, the problem is revisited considering the presence of a strong clutter. Numerical examples are then presented in Section IV to show the accuracy of the proposed method in both the absence and presence of the clutter. Finally, Section V concludes the paper.

Throughout the paper, we use the following notations:

i	Imaginary unit ($\sqrt{-1}$)
$\mathbb{C}$	The set of all complex numbers
$\mathbb{Z}^+$	The set of all positive integers
$\mathrm{Re}[\cdot]$	Real part of a complex number
$\mathrm{Im}[\cdot]$	Imaginary part of a complex number
$\mathrm{diag}\{\cdot\}$	The diagonal elements of a matrix.
$\|\cdot\|_0$	The ℓ_0-norm.
$\|\cdot\|_1$	The ℓ_1-norm
$\otimes$	The Kronecker product
$\odot$	The Hadamard product
$\mathrm{vec}(\cdot)$	The column-wise vectorizing operator for a matrix

[2]This part of the paper was partially presented in [29].

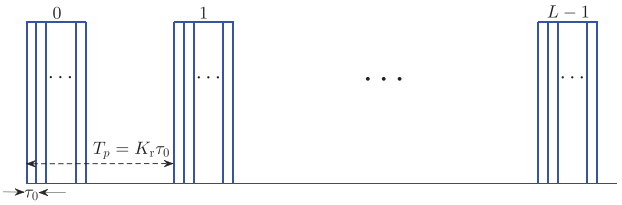

Fig. 1. Transmitted multipulse intracoded signal.

II. CLUTTER-FREE SCENARIO

A. Problem Formulation

Consider a pulse-Doppler radar under a single-input single-output setup. Then, the transmitted multipulse intracoded signal (shown in Fig. 1) is given by

$$s_{\mathrm{T}}(t) = \sum_{\ell=0}^{L-1}\sum_{n=0}^{N-1} c_n\, p(t - n\tau_0 - \ell T_p) \tag{1}$$

where $p(\cdot)$ is the basic subpulse with width τ_0, N is the number of subpulses in each pulse, L is the number of pulses, and $\{c_n\}_{n=0}^{N-1}$ is the code sequence for all pulses, i.e.,

$$\forall \ell = 0, \ldots, L-1, \qquad c_{n,\ell} = c_n. \tag{2}$$

Now suppose that the range and Doppler domains of the radar are grided into K_{r} and K_{d} bins, respectively. Then, at the receiver, we have

$$\begin{aligned} s_{\mathrm{Rec}}(t) &= \sum_{k_{\mathrm{r}}=1}^{K_{\mathrm{r}}}\sum_{k_{\mathrm{d}}=1}^{K_{\mathrm{d}}} \alpha_{k_{\mathrm{r}}k_{\mathrm{d}}} s_T(t - \tau_{k_{\mathrm{r}}}) e^{j\omega_{k_{\mathrm{d}}}t} + \epsilon(t) \\ &= \sum_{k_{\mathrm{r}},k_{\mathrm{d}}}\sum_{\ell,n} \alpha_{k_{\mathrm{r}}k_{\mathrm{d}}} c_n\, p(t - n\tau_0 - \ell T_p - \tau_{k_{\mathrm{r}}}) e^{j\omega_{k_{\mathrm{d}}}t} + \epsilon(t) \end{aligned} \tag{3}$$

where $\tau_{k_{\mathrm{r}}}$, $\omega_{k_{\mathrm{d}}}$, and $\alpha_{k_{\mathrm{r}}k_{\mathrm{d}}}$ are the time delay, Doppler frequency, and the (complex-valued) gain associated with the target with the index pair $(k_{\mathrm{r}}, k_{\mathrm{d}})$ in the range/Doppler domain, respectively, and $\epsilon(t)$ is the additive noise. Define the gain matrix

$$\boldsymbol{\alpha} \triangleq \begin{bmatrix} \alpha_{11} & \cdots & \alpha_{1K_{\mathrm{d}}} \\ \vdots & \ddots & \vdots \\ \alpha_{K_{\mathrm{r}}1} & \cdots & \alpha_{K_{\mathrm{r}}K_{\mathrm{d}}} \end{bmatrix} \tag{4}$$

and let

$$\mathbf{f}(t) \triangleq \begin{bmatrix} \sum_{\ell=0}^{L-1}\sum_{n=0}^{N-1} c_n\, p(t - n\tau_0 - \ell T_p - \tau_1) \\ \vdots \\ \sum_{\ell=0}^{L-1}\sum_{n=0}^{N-1} c_n\, p(t - n\tau_0 - \ell T_p - \tau_{K_{\mathrm{r}}}) \end{bmatrix} \tag{5}$$

where $T_p = K_{\mathrm{r}}\tau_0$. Defining

$$\boldsymbol{\phi}(t) \triangleq [e^{j\omega_1 t}, \ldots, e^{j\omega_{K_{\mathrm{d}}}t}]^T \tag{6}$$

the received signal can be rewritten as follows:

$$s_{\mathrm{Rec}}(t) = \mathbf{f}^T(t)\boldsymbol{\alpha}\boldsymbol{\phi}(t) + \epsilon(t) \tag{7}$$

where $(\cdot)^T$ denotes the transpose.

In order to quantize the received signal, it is compared to a time-varying threshold $h(t) \triangleq h_{\mathrm{R}}(t) + ih_{\mathrm{I}}(t) \in \mathbb{C}$, and

the sign of the resulting difference is observed for the real and imaginary parts. Let $y(t) \triangleq y_{\mathrm{R}}(t) + i y_{\mathrm{I}}(t)$ denote the observed data at time t, i.e.,

$$\begin{aligned} y_{\mathrm{R}}(t) &= \mathrm{sgn}(\mathrm{Re}\left[s_{\mathrm{Rec}}(t)\right] - h_{\mathrm{R}}(t)) \\ &= \mathrm{sgn}\left(\mathrm{Re}\left[\mathbf{f}^T(t)\boldsymbol{\alpha}\boldsymbol{\phi}(t) + \epsilon(t)\right] - h_{\mathrm{R}}(t)\right) \end{aligned} \tag{8}$$

and

$$\begin{aligned} y_{\mathrm{I}}(t) &= \mathrm{sgn}(\mathrm{Im}\left[s_{\mathrm{Rec}}(t)\right] - h_{\mathrm{I}}(t)) \\ &= \mathrm{sgn}\left(\mathrm{Im}\left[\mathbf{f}^T(t)\boldsymbol{\alpha}\boldsymbol{\phi}(t) + \epsilon(t)\right] - h_{\mathrm{I}}(t)\right) \end{aligned} \tag{9}$$

in which $\mathrm{Re}[\cdot]$ and $\mathrm{Im}[\cdot]$ denote the real and imaginary parts, respectively, and

$$\mathrm{sgn}(x) = \begin{cases} 1 & x \geq 0 \\ -1 & x < 0 \end{cases}. \tag{10}$$

Next, assume that M samples are captured at times $t_1, \ldots, t_M$, with a rate of r/τ_0 ($r \in \mathbb{Z}^+$) samples-per-second according to

$$t_m = m\frac{\tau_0}{r}, \qquad m = 1, \ldots, M \tag{11}$$

where τ_0 is the basic subpulse duration as depicted in Fig. 1. In the above sampling scheme, $r = 1$ corresponds to the Nyquist sampling, and $r \geq 2$ therefore denotes the over-sampling rate. Let $\mathbf{h} \triangleq \mathbf{h}_{\mathrm{R}} + i\mathbf{h}_{\mathrm{I}}$, $\boldsymbol{\epsilon}$, and $\mathbf{y} \triangleq \mathbf{y}_{\mathrm{R}} + i\mathbf{y}_{\mathrm{I}}$, respectively, denote the vector of the thresholds, the vector of the additive noise samples, and the vector of the quantized observed data, i.e.,

$$\begin{cases} \mathbf{h} \triangleq [h(t_1), \ldots, h(t_M)]^T \\ \boldsymbol{\epsilon} \triangleq [\epsilon(t_1), \ldots, \epsilon(t_M)]^T \\ \mathbf{y} \triangleq [y(t_1), \ldots, y(t_M)]^T \end{cases}. \tag{12}$$

Defining

$$\mathbf{F} \triangleq \left[\mathbf{f}(t_1)\middle|\mathbf{f}(t_2)\middle|\cdots\middle|\mathbf{f}(t_M)\right]^T \tag{13}$$

and

$$\boldsymbol{\Phi} \triangleq [\boldsymbol{\phi}(t_1)|\boldsymbol{\phi}(t_2)|\cdots|\boldsymbol{\phi}(t_M)] \tag{14}$$

the observed data can be expressed compactly as follows:

$$\begin{cases} \mathbf{y}_{\mathrm{R}} = \mathrm{sgn}(\mathrm{Re}\left[\mathrm{diag}\{\mathbf{F}\boldsymbol{\alpha}\boldsymbol{\Phi}\} + \boldsymbol{\epsilon}\right] - \mathbf{h}_{\mathrm{R}}) \\ \mathbf{y}_{\mathrm{I}} = \mathrm{sgn}(\mathrm{Im}\left[\mathrm{diag}\{\mathbf{F}\boldsymbol{\alpha}\boldsymbol{\Phi}\} + \boldsymbol{\epsilon}\right] - \mathbf{h}_{\mathrm{I}}) \end{cases} \tag{15}$$

where $\mathrm{diag}\{\cdot\}$ gives the diagonal elements of a matrix.

Now, the problem is to estimate the matrix $\boldsymbol{\alpha}$ from the quantized observed data, i.e., $\mathbf{y}$.

B. Proposed Solution

To deal with the aforementioned problem, we begin by vectorizing the matrix $\boldsymbol{\alpha}$ as follows:

$$\begin{aligned} \widetilde{\boldsymbol{\alpha}} &\triangleq \mathrm{vec}(\boldsymbol{\alpha}) \\ &= [\alpha_{11}, \ldots, \alpha_{K_{\mathrm{r}}1}, \ldots \alpha_{1K_{\mathrm{d}}}, \ldots \alpha_{K_{\mathrm{r}}K_{\mathrm{d}}}]^T. \end{aligned} \tag{16}$$

It is verified that $\mathrm{diag}\{\mathbf{F}\boldsymbol{\alpha}\boldsymbol{\Phi}\}$ can be recast as

$$\begin{aligned} &\mathrm{diag}\{\mathbf{F}\boldsymbol{\alpha}\boldsymbol{\Phi}\} \\ &= \begin{bmatrix} e^{j\omega_1 t_1}\mathbf{f}^T(t_1) & \cdots & e^{j\omega_{K_{\mathrm{d}}} t_1}\mathbf{f}^T(t_1) \\ e^{j\omega_1 t_2}\mathbf{f}^T(t_2) & \cdots & e^{j\omega_{K_{\mathrm{d}}} t_2}\mathbf{f}^T(t_2) \\ \vdots & \vdots & \vdots \\ e^{j\omega_1 t_M}\mathbf{f}^T(t_M) & \cdots & e^{j\omega_{K_{\mathrm{d}}} t_M}\mathbf{f}^T(t_M) \end{bmatrix} \widetilde{\boldsymbol{\alpha}} \\ &= (\mathbf{1}_{1\times K_{\mathrm{d}}} \otimes \mathbf{F}) \odot (\boldsymbol{\Phi}^T \otimes \mathbf{1}_{1\times K_{\mathrm{r}}})\widetilde{\boldsymbol{\alpha}} \end{aligned} \tag{17}$$

where $\otimes$ and $\odot$ are the Kronecker and Hadamard products, respectively, and $\mathbf{1}$ is a matrix of all ones.

Thus, the observed quantized data can be expressed as

$$\begin{cases} \mathbf{y}_R = \mathrm{sgn}\left(\mathrm{Re}[\widetilde{\mathbf{F}}\widetilde{\boldsymbol{\alpha}} + \boldsymbol{\epsilon}] - \mathbf{h}_R\right) \\ \mathbf{y}_I = \mathrm{sgn}\left(\mathrm{Im}[\widetilde{\mathbf{F}}\widetilde{\boldsymbol{\alpha}} + \boldsymbol{\epsilon}] - \mathbf{h}_I\right) \end{cases} \tag{18}$$

in which

$$\widetilde{\mathbf{F}} \triangleq (\mathbf{1}_{1\times K_{\mathrm{d}}} \otimes \mathbf{F}) \odot (\boldsymbol{\Phi}^T \otimes \mathbf{1}_{1\times K_{\mathrm{r}}}) \tag{19}$$

and $\widetilde{\boldsymbol{\alpha}}$ has been defined in (16). Noting the sparsity of the targets in the range and Doppler domains, we expect that many of the components of the vector $\widetilde{\boldsymbol{\alpha}}$ will be zero. Thus, the problem is to find a sparse vector $\widetilde{\boldsymbol{\alpha}}$, consistent with the measurement with small fitting error. The problem is therefore expressed in a form similar to the one in [27] and [28], and it thus leads to the following optimization problem:

$$\begin{aligned} \min_{\widetilde{\boldsymbol{\alpha}},\mathbf{z}} \quad & \|\mathbf{z}\|_2 + \lambda\|\widetilde{\boldsymbol{\alpha}}\|_0 \\ \text{s.t.} \quad & \mathbf{y}_R \odot (\mathrm{Re}[\widetilde{\mathbf{F}}\widetilde{\boldsymbol{\alpha}} + \mathbf{z}] - \mathbf{h}_R) \geq 0 \\ & \mathbf{y}_I \odot (\mathrm{Im}[\widetilde{\mathbf{F}}\widetilde{\boldsymbol{\alpha}} + \mathbf{z}] - \mathbf{h}_I) \geq 0 \end{aligned} \tag{20}$$

where $\|\cdot\|_0$ is the zero norm, $\mathbf{z}$ is the fitting error, and λ is a parameter, which adjusts the sparsity of the result. Note that the zero norm (with which the problem is hard to solve) can be well approximated by the ℓ_1-Norm ($\|\cdot\|_1$) that makes the problem convex and tractable [34].

In the sequel, without loss of generality, we assume that the Doppler grids are equally spaced, i.e.,

$$\omega_{k_{\mathrm{d}}} = -\omega_{\mathrm{D}} + (k_{\mathrm{d}} - 1)\Delta, \quad \text{for } k_{\mathrm{d}} = 1, \ldots, K_{\mathrm{d}} \tag{21}$$

where ω_{D} is the maximum possible Doppler frequency of a potential target, and $\Delta = \frac{2\omega_{\mathrm{D}}}{K_{\mathrm{d}}-1}$. In this way,

we have

$$\boldsymbol{\phi}(t) = [e^{-j\omega_{\mathrm{D}}t},\ e^{-j(\omega_{\mathrm{D}}-\Delta)t}, \ldots, e^{j(\omega_{\mathrm{D}}-\Delta)t},\ e^{j\omega_{\mathrm{D}}t}]^T. \quad (22)$$

Then, from (22) and (11), it can be seen that $\boldsymbol{\Phi}$ is a Vandermonde matrix given by

$$\boldsymbol{\Phi} = \left[\boldsymbol{\phi}\,\middle|\,\boldsymbol{\phi}^{(2)}\,\middle|\cdots\middle|\,\boldsymbol{\phi}^{(M)}\right] \quad (23)$$

with $\boldsymbol{\phi}^{(i)}$ denoting the i'th Hadamard-power of the vector $\boldsymbol{\phi}$

$$\boldsymbol{\phi} = \left[e^{-j\omega_D\frac{\tau_0}{r}},\ e^{-j(\omega_D-\Delta)\frac{\tau_0}{r}}, \ldots,\ e^{j\omega_D\frac{\tau_0}{r}}\right]^T. \quad (24)$$

Similarly, we assume that the range grids are also equally spaced such that they represent delay steps equal to τ_0/r, i.e.,

$$\tau_{k_{\mathrm{r}}} = k_{\mathrm{r}}\frac{\tau_0}{r}, \quad k_{\mathrm{r}} = 1, \ldots, K_{\mathrm{r}}. \quad (25)$$

Before we proceed, let us look into the structure of the matrix $\mathbf{F}$. According to the following lemma, each element in $\mathbf{F}$ is either zero or c_n, for some $n = 0, \ldots, N-1$.

LEMMA 1 Let $\mathbf{F}[m, k_{\mathrm{r}}]$ denote the element in the m'th row and k_{r}'th column of $\mathbf{F}$, and assume that $K_{\mathrm{r}} > N$. Then, for all $m = 1, \ldots, M$, and all $k_{\mathrm{r}} = 1, \ldots, K_{\mathrm{r}}$, we have

$$\mathbf{F}[m, k_{\mathrm{r}}] \in \{c_0, c_1, \ldots, c_{N-1}, 0\}.$$

PROOF See Appendix A for the proof. ■

Based on the above lemma, it is not hard to characterize the structure of $\mathbf{F}$ according to the following proposition.

PROPOSITION 1 Consider the element in the m'th row and k_{r}'th column of $\mathbf{F}$, denoted by $\mathbf{F}[m, k_{\mathrm{r}}]$. Then, we have

$$\mathbf{F}[m, k_{\mathrm{r}}] = c_n, \quad n \in \{0, \ldots, N-1\}$$

if and only if the following equation is satisfied for some value of $x \in \{0, 1, \ldots, r-1\}$:

$$(m \bmod rK_{\mathrm{r}}) - k_{\mathrm{r}} = rn + x$$

where $(m \bmod rK_{\mathrm{r}})$ denotes the remainder of m divided by rK_{r}.

PROOF According to Lemma 1, and following the lines of its proof given in Appendix A, the proof is immediate. ■

For $n = 0, \ldots, N-1$, defining $\mathbf{c}_n \triangleq c_n\mathbf{1}_{r\times 1}$, and assuming reasonably that $K_r > rN$, from (2), (5), (11), (13), and (25), it can be seen that with $M = (L-1)rK_{\mathrm{r}} + rN + K_{\mathrm{r}} - 1$, the matrix $\mathbf{F}$ is an $M \times K_{\mathrm{r}}$ matrix given by

$$\mathbf{F} = \begin{bmatrix}
\mathbf{c}_0 & & & & 1 \\
\vdots & \ddots & & & \\
\mathbf{c}_{N-1} & \ddots & \ddots & & r(N-1)+1 \\
 & \ddots & \ddots & \mathbf{c}_0 & K_r \\
 & & \ddots & \vdots & \\
 & & & \mathbf{c}_{N-1} & K_r + rN - r \\
\mathbf{c}_0 & & & & rK_r + 1 \\
\vdots & \ddots & & & \\
\mathbf{c}_{N-1} & \ddots & \ddots & & \\
 & \ddots & \ddots & \mathbf{c}_0 & \\
 & & \ddots & \vdots & \\
 & & & \mathbf{c}_{N-1} & \\
 & \vdots & & & \\
 & & \vdots & & \\
\mathbf{c}_0 & & & & (L-1)rK_r + 1 \\
\vdots & \ddots & & & \\
\mathbf{c}_{N-1} & \ddots & \ddots & & \\
 & \ddots & \ddots & \mathbf{c}_0 & \\
 & & \ddots & \vdots & \\
 & & & \mathbf{c}_{N-1} &
\end{bmatrix} \quad (26)$$

in which the entries outside the shown repetitive diagonal boxes are all zero, and the column on the right-hand side of the matrix is the starting row index for the relevant inline entry.[3]

Having characterized $\mathbf{F}$ and $\boldsymbol{\Phi}$, we are now ready to evaluate the performance of the proposed method, by numerically solving the minimization problem in (20).

III. PRESENCE OF CLUTTER

Adding the clutter effect to the same setup considered in the previous section, the received signal can be represented

[3]Considering $K_r > rN$, the only case in which the diagonal boxes overlap is with $r = 1$ for which $rK_r + 1 < K_r + rN$.

by

$$
\begin{aligned}
&s_{\text{Rec}}(t)\\
&\quad=\sum_{k_\text{r}=1}^{K_\text{r}}\sum_{k_\text{d}=1}^{K_\text{d}}(\alpha_{k_\text{r}k_\text{d}}+\beta_{k_\text{r}k_\text{d}})s_\text{T}(t-\tau_{k_\text{r}})e^{j\omega_{k_\text{d}}t}+\epsilon(t)\\
&\quad=\sum_{k_\text{r},k_\text{d}}\sum_{\ell,n}(\alpha_{k_\text{r}k_\text{d}}+\beta_{k_\text{r}k_\text{d}})c_n\,p(t-n\tau_0-\ell T_p-\tau_{k_\text{r}})e^{j\omega_{k_\text{d}}t}\\
&\qquad+\epsilon(t)
\end{aligned}
\tag{27}
$$

where $\alpha_{k_\text{r}k_\text{d}}$ is the complex-valued gain corresponding to the target with the index pair (k_r, k_d) in the range/Doppler domain, and the newly added term $\beta_{k_\text{r}k_\text{d}}$ is the complex-valued clutter component associated with the range-Doppler index-pair (k_r, k_d). Therefore, similar to (7), the received signal is given compactly as follows:

$$
s_{\text{Rec}}(t)=\mathbf{f}^T(t)(\boldsymbol{\alpha}+\boldsymbol{\beta})\boldsymbol{\phi}(t)+\epsilon(t) \tag{28}
$$

in which $\mathbf{f}^T(t)$ and $\boldsymbol{\phi}(t)$ are previously defined in (5) and (6), and

$$
\boldsymbol{\beta}\triangleq\begin{bmatrix}\beta_{11} & \cdots & \beta_{1K_\text{d}}\\ \vdots & \ddots & \vdots\\ \beta_{K_\text{r}1} & \cdots & \beta_{K_\text{r}K_\text{d}}\end{bmatrix}. \tag{29}
$$

In what follows, we first discuss the case of weak clutter; then we move on to the case of strong clutter which is the main focus of this section.

A. Weak Clutter

In the case of weak clutter, the clutter can be treated as an additive noise. Specifically, the received signal is rewritten as

$$
s_{\text{Rec}}(t)=\mathbf{f}^T(t)\boldsymbol{\alpha}\boldsymbol{\phi}(t)+\sigma(t) \tag{30}
$$

in which $\sigma(t)=\mathbf{f}^T(t)\boldsymbol{\beta}\boldsymbol{\phi}(t)+\epsilon(t)$ can be considered as an additive colored noise. Note that in the formulation of (20), the variable $\mathbf{z}$ represents the fitting error, which is a result of both the additive noise and the signal-dependent quantization noise, which is in fact colored. Therefore, it is expected that by merging the weak clutter effect into the fitting error, the same formulation and approach can be effectively used. Indeed, the simulation results confirm this fact. Therefore, the case of weak clutter shall not be a major concern in our proposed method, and therefore, in the remainder of this section, we focus on the case of strong clutter.

B. Strong Clutter

We begin by reformulating the received signal in (28). Let $\boldsymbol{\xi}\triangleq\boldsymbol{\alpha}+\boldsymbol{\beta}$. Then, similar to the clutter-free scenario, the observed quantized data can be stated as

$$
\begin{cases}\mathbf{y}_\text{R}=\text{sgn}(\text{Re}\left[\text{diag}\{\mathbf{F}\boldsymbol{\xi}\boldsymbol{\Phi}\}+\boldsymbol{\epsilon}\right]-\mathbf{h}_\text{R})\\ \mathbf{y}_\text{I}=\text{sgn}(\text{Im}\left[\text{diag}\{\mathbf{F}\boldsymbol{\xi}\boldsymbol{\Phi}\}+\boldsymbol{\epsilon}\right]-\mathbf{h}_\text{I})\end{cases} \tag{31}
$$

or equivalently by

$$
\begin{cases}\mathbf{y}_\text{R}=\text{sgn}\left(\text{Re}[\widetilde{\mathbf{F}}\widetilde{\boldsymbol{\xi}}+\boldsymbol{\epsilon}]-\mathbf{h}_\text{R}\right)\\ \mathbf{y}_\text{I}=\text{sgn}\left(\text{Im}[\widetilde{\mathbf{F}}\widetilde{\boldsymbol{\xi}}+\boldsymbol{\epsilon}]-\mathbf{h}_\text{I}\right)\end{cases} \tag{32}
$$

where $\widetilde{\mathbf{F}}$ is defined in (19), and $\widetilde{\boldsymbol{\xi}}=\text{vec}(\boldsymbol{\xi})$. Without loss of generality suppose that K_d is an odd number given by $2c+1$. Then, the matrix $\boldsymbol{\xi}$ can be rewritten as shown at the bottom of this page in (33), where $0\le\delta<c$ is selected according to the clutter spectral spread in a way that the major components of the clutter fall in $\boldsymbol{\xi}_0$. This is because, in the representation of the strong clutter effect, the matrix $\boldsymbol{\beta}$ has its significant components within the central columns, i.e., about the zero Doppler frequency. This will be further explained below in Remark 2. The matrix $\widetilde{\mathbf{F}}$ has $K_\text{d}=2c+1$ columns; let $\widetilde{\mathbf{F}}_-$, $\widetilde{\mathbf{F}}_0$, and $\widetilde{\mathbf{F}}_+$ denote the first $c-\delta$ columns, the central $2\delta+1$ columns, and the last $c-\delta$ columns of $\widetilde{\mathbf{F}}$, respectively. Then, we can write

$$
\widetilde{\mathbf{F}}\widetilde{\boldsymbol{\xi}}=\left[\widetilde{\mathbf{F}}_-\middle|\,\widetilde{\mathbf{F}}_0\middle|\,\widetilde{\mathbf{F}}_+\right]\begin{bmatrix}\widetilde{\boldsymbol{\xi}}_-\\ ---\\ \widetilde{\boldsymbol{\xi}}_0\\ ---\\ \widetilde{\boldsymbol{\xi}}_+\end{bmatrix} \tag{34}
$$

where $\widetilde{\boldsymbol{\xi}}_-=\text{vec}(\boldsymbol{\xi}_-)$, $\widetilde{\boldsymbol{\xi}}_0=\text{vec}(\boldsymbol{\xi}_0)$, and $\widetilde{\boldsymbol{\xi}}_+=\text{vec}(\boldsymbol{\xi}_+)$. Defining

$$
\begin{cases}\widetilde{\mathbf{F}}_\text{cf}\triangleq\left[\widetilde{\mathbf{F}}_-\middle|\,\widetilde{\mathbf{F}}_+\right]\\ \widetilde{\boldsymbol{\xi}}_\text{cf}\triangleq\begin{bmatrix}\widetilde{\boldsymbol{\xi}}_-\\ --\\ \widetilde{\boldsymbol{\xi}}_+\end{bmatrix}\end{cases} \tag{35}
$$

where the subscript "cf" stands for clutter-free, it can be verified that the observed quantized data can be restated as follows:

$$
\begin{cases}\mathbf{y}_\text{R}=\text{sgn}\left(\text{Re}\left[\widetilde{\mathbf{F}}_\text{cf}\widetilde{\boldsymbol{\xi}}_\text{cf}+\widetilde{\mathbf{F}}_0\widetilde{\boldsymbol{\xi}}_0+\boldsymbol{\epsilon}\right]-\mathbf{h}_\text{R}\right)\\ \mathbf{y}_\text{I}=\text{sgn}\left(\text{Im}\left[\widetilde{\mathbf{F}}_\text{cf}\widetilde{\boldsymbol{\xi}}_\text{cf}+\widetilde{\mathbf{F}}_0\widetilde{\boldsymbol{\xi}}_0+\boldsymbol{\epsilon}\right]-\mathbf{h}_\text{I}\right)\end{cases}. \tag{36}
$$

$$
\boldsymbol{\xi}\triangleq\left[\boldsymbol{\xi}_-\middle|\,\boldsymbol{\xi}_0\middle|\,\boldsymbol{\xi}_+\right]=\left[\begin{array}{ccc|\overbrace{ccccc}^{\text{strong clutter-affected}}|ccc}
\xi_{1,1} & \cdots & \xi_{1,c-\delta-1} & \xi_{1,c-\delta} & \cdots & \xi_{1,c} & \cdots & \xi_{1,c+\delta} & \xi_{1,c+\delta+1} & \cdots & \xi_{1,K_\text{d}}\\
\vdots & \vdots & \vdots & \vdots & \vdots & \vdots & \vdots & \vdots & \vdots & \vdots & \vdots\\
\xi_{K_\text{r},1} & \cdots & \xi_{K_\text{r},c-\delta-1} & \xi_{K_\text{r},c-\delta} & \cdots & \xi_{K_\text{r},c} & \cdots & \xi_{K_\text{r},c+\delta} & \xi_{K_\text{r},c+\delta+1} & \cdots & \xi_{K_\text{r},K_\text{d}}
\end{array}\right] \tag{33}
$$

REMARK 1 In our formulation, the column indices of $\boldsymbol{\xi}$ represent the Doppler frequency shift ω_d. According to (21), the matrix $\boldsymbol{\xi}_0$ corresponds to Doppler frequencies within the interval

$$-\frac{\omega_{\mathrm{D}}}{2c}\delta \leq \omega_{\mathrm{d}} \leq \frac{\omega_{\mathrm{D}}}{2c}\delta$$

where ω_{D} is the maximum Doppler frequency shift of a potential target. ■

REMARK 2 Frequently in practice, clutter strength decays as the Doppler frequency increases [33]. Therefore, we can assume that the significant components of the clutter effect are confined to a maximum Doppler frequency $\omega_{\mathrm{d}}^{\star}$, beyond which the clutter is weak and can thus be treated as mentioned in Section III-A. In the above formulation, the parameter δ is set such that[4]

$$\frac{\omega_{\mathrm{D}}}{2c}\delta \geq \omega_{\mathrm{d}}^{\star}.$$ ■

REMARK 3 According to the above two remarks, the vector $\widetilde{\boldsymbol{\xi}}$ has at most $(2\delta+1)K_{\mathrm{r}}+N_t$ nonzero elements (out of $K_{\mathrm{r}}K_{\mathrm{d}}$ total elements), where N_t is the number of targets. Therefore, by choosing K_{d} large enough, *at a fixed Doppler resolution* Δ, the ratio

$$\frac{(2\delta+1)K_{\mathrm{r}}+N_t}{K_{\mathrm{r}}K_{\mathrm{d}}} \simeq \frac{2\delta+1}{K_{\mathrm{d}}}$$

can be kept small enough, leading to a relatively sparse vector. This paves the way to dealing with the strong clutter. ■

DISCUSSION 1 The restricted isometry property (RIP) of the measurement matrix serves as a guarantee for universal recovery of sparse signals in traditional CS, where the focus is on undersampling (with or without quantization). In our scenario however, the term *compressive* relates to reducing the bit-depth of the samples, and not the number of the samples. This is the source of a distinction in the theory of the two. One example of such difference is the concern on the mutual coherence of the measurement vectors (columns of the measurement matrix). Indeed, in traditional CS where the focus is on the minimum number of samples for perfect recovery of the sparse signal, the coherence parameter is a major concern because the minimum required samples for perfect recovery is linearly proportional to the coherence parameter [35]. In our study however, having reduced the bit-depth to one, we worry less about the number of samples, and thus the coherence parameter, as long as the system works efficiently.

From the literature on RIP, we know the following theorem, which states a necessary condition for the RIP [35].

THEOREM Let A be an $M \times D$ matrix that satisfies the RIP of order $2K$ with a constant $\delta \in (0, \frac{1}{2}]$, then

$$M > CK\log\left(\frac{D}{K}\right) \tag{37}$$

where $C \approx 0.28$.

[4]In practice, δ and $K_{\mathrm{d}} = 2c+1$ are codesigned to meet the practical requirements.

However, we must note that as stated in [35] and [36], the RIP itself is merely a sufficient but not necessary condition for CS. Indeed, the RIP does not hold in many applications where CS is successfully used. This includes some of the flagships of CS like magnetic resonance imaging. The RIP guarantees the ability to recover all K-sparse vectors x using the values of Φx, which is commonly known as uniform recovery or universality. Expecting uniform recovery (universality) is unrealistic in a variety of situations, where we might only care about particular realizations of the sparse signal.

In our formulation, the matrix $\tilde{\mathbf{F}}$ is an $M \times K_{\mathrm{r}}K_{\mathrm{d}}$ matrix, where $M = (L-1)rK_{\mathrm{r}} + rN + K_{\mathrm{r}} - 1$. Moreover, the support of the signal-and-clutter vector is given by $(2\delta+1)K_{\mathrm{r}}$. Therefore, the condition in (37) can be rephrased as follows:

$$[(L-1)r+1]K_{\mathrm{r}} + rN - 1 > C(2\delta+1)K_{\mathrm{r}}\log\left(\frac{K_{\mathrm{d}}}{2\delta+1}\right). \tag{38}$$

Thus, despite the above explanations, in order to satisfy (38), it suffices that $(L-1)r > \log\left(\frac{K_{\mathrm{d}}}{2\delta+1}\right)$, which will be the case, in all the examples studied in Section IV-B.

Finally, note that as explicitly stated in Remark 3, K_{d} is to be chosen *large enough*, which does not imply unthoughtful increase in K_{d}, especially that the choice of K_{d} affects L and consequently M in our study. Therefore, it is a matter of tradeoff, which adds to the beauty and delicacy of the concept in this problem. ■

Remark 3 is our key to tackling the problem under strong clutter effect. Accordingly, one way for dealing with the clutter-affected scenario is to perform a sparse estimation of *signal-and-clutter* (i.e., to obtain $\widehat{\widetilde{\boldsymbol{\xi}}}$), discard the estimated (clutter) components within the clutter Doppler zone $-\omega_{\mathrm{d}}^{*} \leq \omega_{\mathrm{d}} \leq \omega_{d}^{*}$ (i.e., to obtain $\widehat{\widetilde{\boldsymbol{\xi}}} \rightarrow \widehat{\widetilde{\boldsymbol{\xi}}}_s$, where $\widehat{\widetilde{\boldsymbol{\xi}}}_s$ is the clutter-discarded version of $\widehat{\widetilde{\boldsymbol{\xi}}}$), and finally locate any targets in the detectable Doppler zone (i.e., to convert the vectorized estimation to the matrix of Doppler-Range pairs $\widehat{\xi}$). This can be performed by considering the following optimization problem:

$$\begin{aligned} \min_{\widetilde{\boldsymbol{\xi}}_{\mathrm{cf}},\widetilde{\boldsymbol{\xi}}_0,\mathbf{z}} \quad & \|\mathbf{z}\|_2 + \lambda_{\mathrm{cf}}\left\|\widetilde{\boldsymbol{\xi}}_{\mathrm{cf}}\right\|_0 + \lambda_0\left\|\widetilde{\boldsymbol{\xi}}_0\right\|_0 \\ \text{s.t.} \quad & \mathbf{y}_{\mathrm{R}} \odot (\mathrm{Re}[\widetilde{\mathbf{F}}_{\mathrm{cf}}\widetilde{\boldsymbol{\xi}}_{\mathrm{cf}} + \widetilde{\mathbf{F}}_0\widetilde{\boldsymbol{\xi}}_0 + \mathbf{z}] - \mathbf{h}_{\mathrm{R}}) \geq 0 \\ & \mathbf{y}_{\mathrm{I}} \odot (\mathrm{Im}[\widetilde{\mathbf{F}}_{\mathrm{cf}}\widetilde{\boldsymbol{\xi}}_{\mathrm{cf}} + \widetilde{\mathbf{F}}_0\widetilde{\boldsymbol{\xi}}_0 + \mathbf{z}] - \mathbf{h}_{\mathrm{I}}) \geq 0 \end{aligned} \tag{39}$$

where the parameters λ_{cf}, λ_0 should be adjusted such that $\lambda_{\mathrm{cf}} > \lambda_0 > 0$. This is because the signal components ($\widetilde{\boldsymbol{\xi}}_{\mathrm{cf}}$) are sparser than the clutter components ($\widetilde{\boldsymbol{\xi}}_0$).

IV. NUMERICAL EXAMPLES AND SIMULATION RESULTS

In this section, we provide numerical examples to evaluate the performance of the proposed method. In all examples, the CAN algorithm [37] is used to produce the complex code $c_0, \ldots, c_{N-1}$. Using ℓ_1-norm approximation in (20) and (39), we use MATLAB's CVX toolbox [38] to find $\widetilde{\boldsymbol{\alpha}}$ and $\widetilde{\boldsymbol{\xi}}$, respectively. We begin with the clutter-free setup.

TABLE I
Parameters in Example 1

N_t	SNR	N	r	$K_{\rm r}$	$K_{\rm d}$	L	τ_0	$\omega_{\rm D}$	λ
4	6 dB	16	2	200	21	5	0.01 ms	2000π rad/sec	1

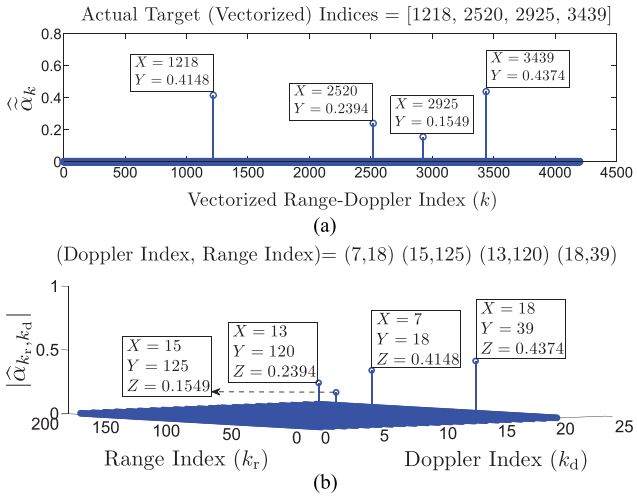

Fig. 2. Sensing performance of the proposed radar system for Example 1. (a) Estimated vectorized target indices $\widehat{\widetilde{\boldsymbol{\alpha}}}$. (b) Range-Doppler representation of the targets.

A. Clutter-Free Scenario

We consider $\mathbf{h}_{\rm R}$ and $\mathbf{h}_{\rm I}$ as independent vectors of i.i.d. random variables uniformly distributed over $[-1,\ 1]$ (which is the range for the normalized amplitude of the reflected signals) and we set $\lambda = 1$.

In the first two examples, the targets are randomly located by producing random i.i.d. delay and Doppler frequency indices. In Example 3, however, we have used the same target indices as those in Example 2, for comparison purposes.

EXAMPLE 1 Consider the scenario with parameters set according to Table I, in which N_t is the number of targets and the SNR is measured with respect to the weakest target. The actual range-Doppler indices of the four targets in this example are (7,18), (15,125), (13,120), and (18, 39). The vectorized indices of the assumed targets are 1218, 2520, 2925, and 3439, respectively. As it can be seen in Fig. 2, the proposed method is able to detect all four targets accurately. □

EXAMPLE 2 Consider the same setup of Example 1 with a lower SNR of 2 dB, and suppose that the actual range-Doppler indices of the targets are randomly set as (16,18), (15,65), (13,83), and (17, 173). As it can be seen in Fig. 3, by decreasing the SNR, an error has occurred in the estimation of the Doppler index for one of the targets. As shown by the red-dashed boxes, the Doppler index of the third target has been estimated incorrectly as 18, instead of the actual index 13. □

EXAMPLE 3 Consider the same scenario in Example 2, but with a higher sampling rate of $r = 3$. As it can be seen in Fig. 4, increasing the sampling rate compensates for the low SNR and improves the sensing performance, such that all four targets are identified accurately. □

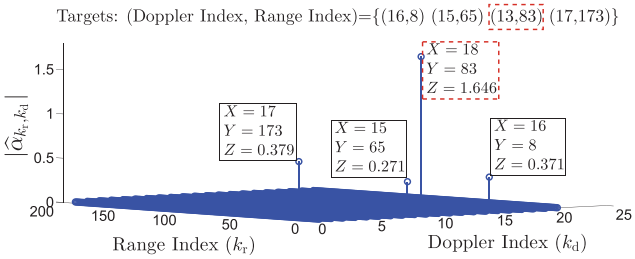

Fig. 3. Performance of the proposed method for Example 2. The erroneous estimated target is shown in dashed box.

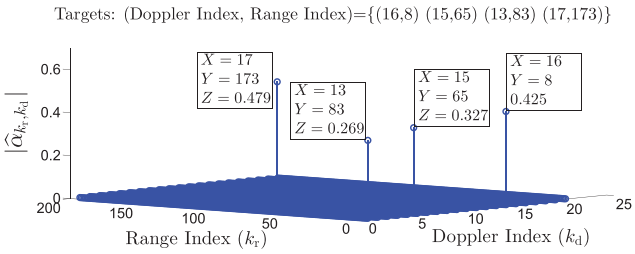

Fig. 4. Sensing performance of the proposed method for Example 3.

TABLE II
Parameters in Example 4

N_t	SNR	N	r	$K_{\rm r}$	$K_{\rm d}$	L	τ_0	$\omega_{\rm D}$	λ
2	0 dB	8	4	20	41	8	0.03 ms	1600π rad/sec	1

The phenomenon observed in Example 3 is similar to the well-known results mentioned in the context of oversampling ADCs (e.g., [30]–[32]).

EXAMPLE 4 In this example, we look into the dynamic range of the targets. Specifically, consider a scenario with parameters set according to Table II and 40 dB difference in the power of the two targets. As it can be seen in Fig. 5(a) and (b), the proposed method is able to resolve the targets even at such high dynamic range. Next, in order to evaluate the average performance of the method, we run 100 independent trials in this setup to calculate the *probability of perfect estimation*, i.e., the probability that both targets are estimated accurately.[5] The procedure is then repeated for $r = 8$ and 16, the result of which is shown in Fig. 5(c), where $A_{\rm strong}$, and $A_{\rm weak}$ denote the amplitude of the strong and weak targets, respectively. As it can be observed, by increasing the sampling rate, the method is able to estimate the targets accurately with a high probability, even at dynamic ranges of up to 40 dB. □

B. Presence of Clutter

In this section, we provide numerical examples to evaluate the performance of the proposed method in the presence of a strong clutter.

[5]Here in this example, it is assumed that the number of targets are known.

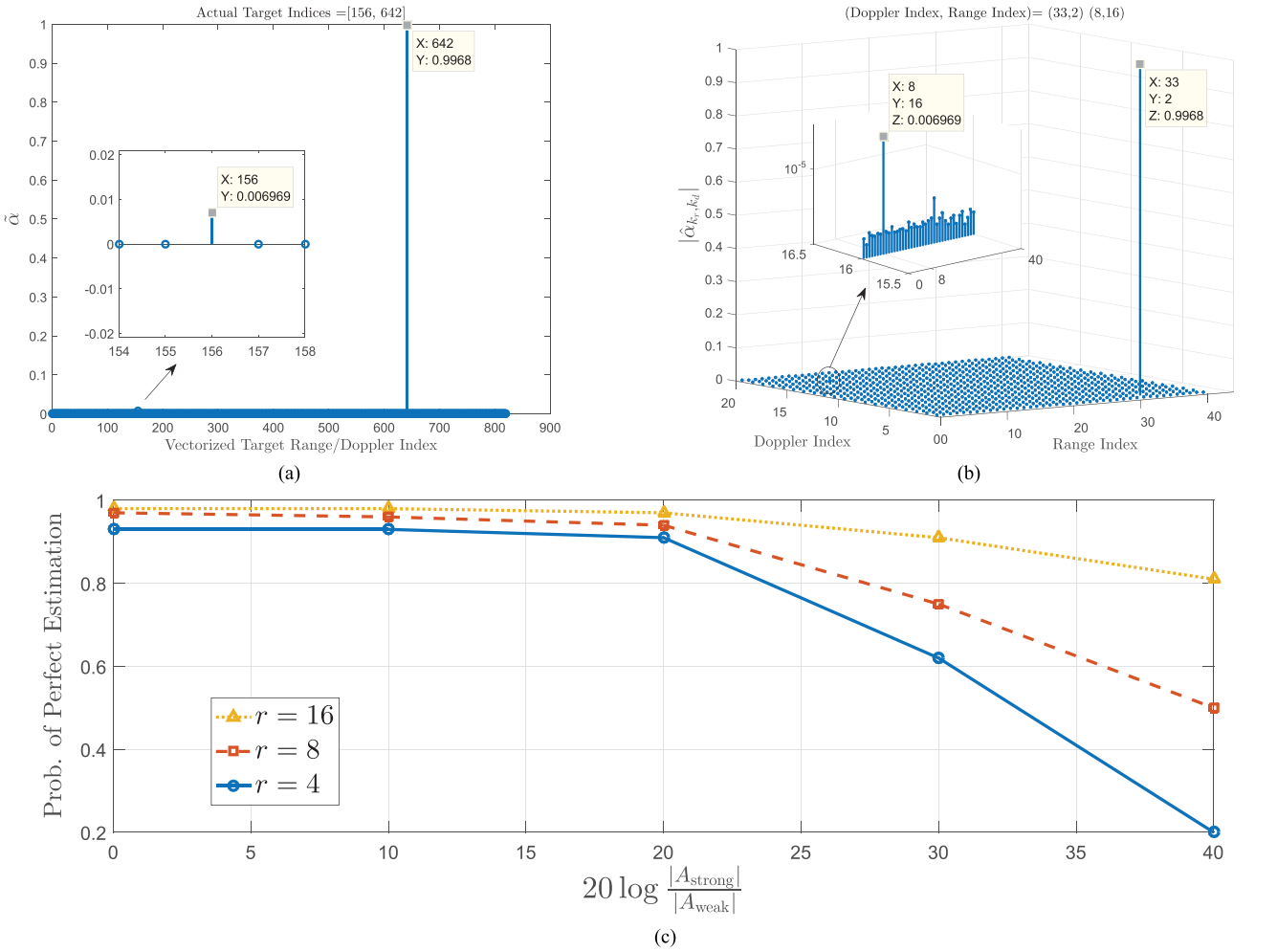

Fig. 5. Sensing performance of the proposed radar sensing in Example 4. (a) Estimated vectorized target indices $\widehat{\widetilde{\boldsymbol{\alpha}}}$. (b) Range-Doppler representation of the targets. (c) Probability of perfect estimation versus the dynamic range of the targets, for different values of $r = 4$, 8, and 16 at 0 dB SNR.

TABLE III
Parameters in Example 5

N_t	SNR	δ	N	r	K_r	K_d	L	τ_0	ω_D	λ_cf	λ_0
1	5 dB	1	8	2	20	41	41	0.03 ms	1600π rad/sec	6/7	1/7

EXAMPLE 5 Suppose that we are faced with a strong clutter, with a clutter-to-signal ratio (CSR) of 20 dB (measured with respect to the weakest signal) at the zero-Doppler frequency, and a decay rate of 0.25 dB/Hz, confined to ± 40 Hz. Now consider a scenario with parameters given in Table III, in which N_t is the number of targets and the SNR is measured with respect to the weakest reflected signal. With K_d set equal to 41, and ω_D equal to 1600π, the strong clutter is confined to the three central columns of $\boldsymbol{\xi}$, i.e., $\delta = 1$, as shown in Fig. 6. Fig. 7(a)–(d) depicts the performance of the proposed method for the considered scenario with a target randomly located at the range-Doppler index (18, 10) (which is index 350 in the vectorized form). As it can be seen, the target has been detected accurately.

EXAMPLE 6 Consider the scenario of the previous example at a lower SNR of 0 dB. As it can be seen in Fig. 8(a)–(d), reducing the SNR has led to an error in the range of the estimated target. One way to overcome this problem is to increase the sampling rate. As it can be seen in Fig. 8(d), by increasing r to 3, the proposed method is able to estimate the target accurately. □

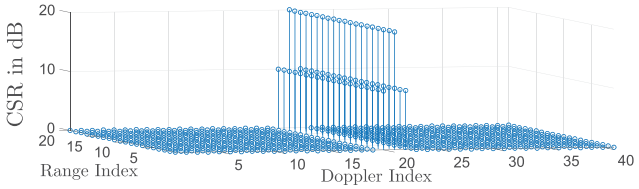

Fig. 6. CSR in Example 5.

EXAMPLE 7 Consider the scenario in Example 6, but with $N_t = 2$, i.e., with two targets located at range-Doppler indices (5, 16) and (18, 10) (i.e., vectorized indices 96 and 350, respectively). As it can be seen in Fig. 9(a)–(d), the proposed method is able to estimate both targets accurately. Now let us consider a case where the two targets have closer indices. For example, suppose that both targets have the same Doppler index of $k_\mathrm{d} = 18$, and range indices

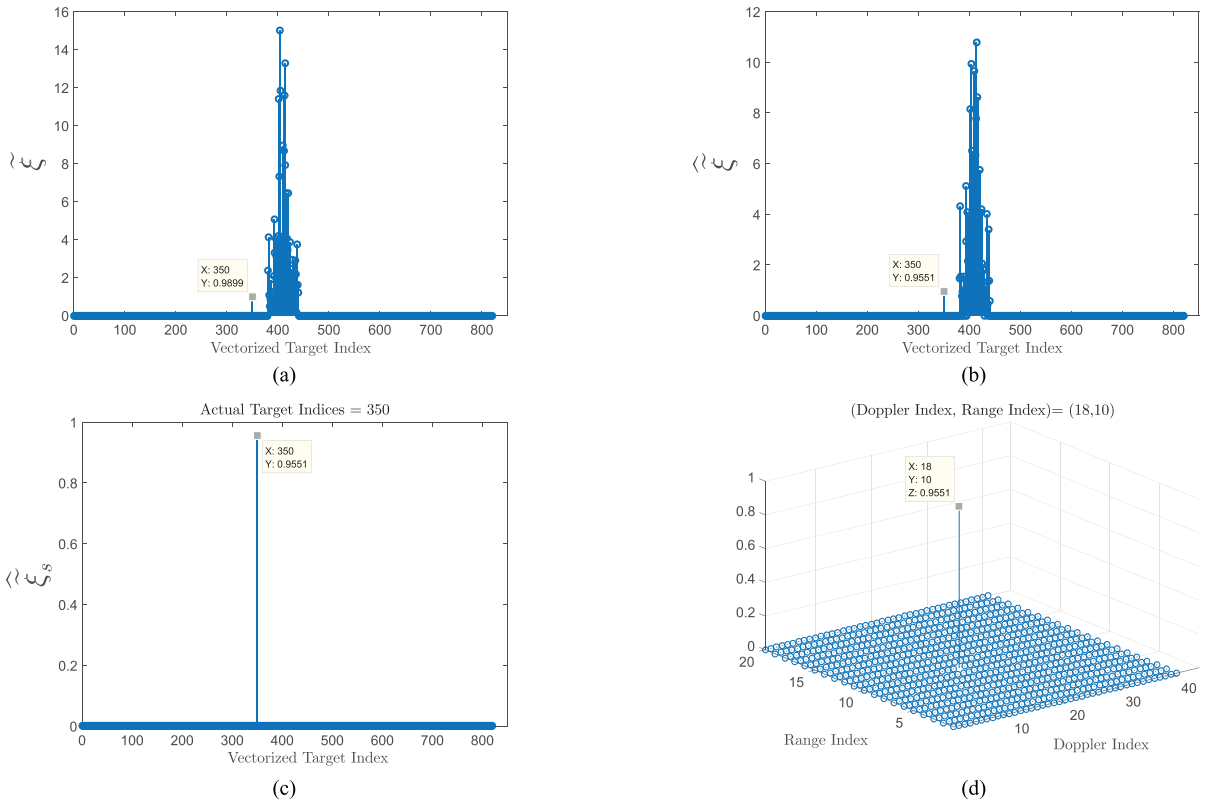

Fig. 7. Performance of the proposed sensing method in Example 5. (a) Actual vectorized target-and-clutter indices $\widetilde{\boldsymbol{\xi}}$. (b) Estimated vectorized target-and-clutter indices $\widehat{\widetilde{\boldsymbol{\xi}}}$. (c) Estimated vectorized target index. (d) Range-Doppler representation of the estimated target.

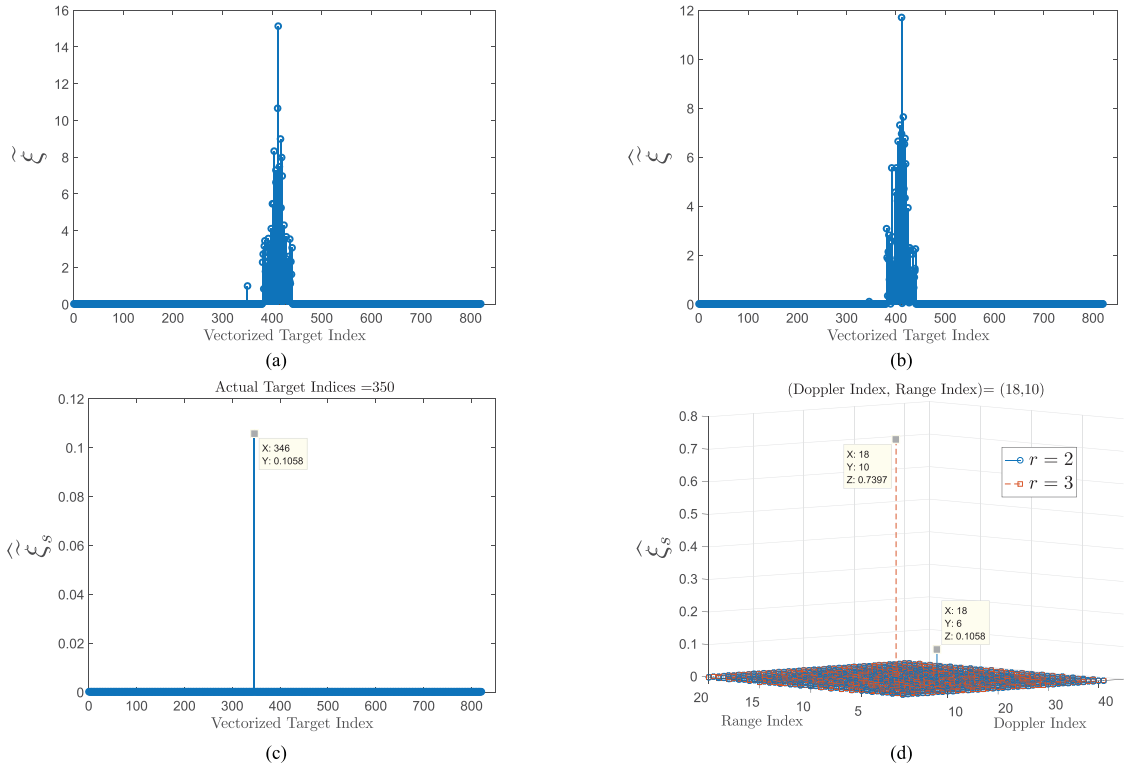

Fig. 8. Performance of the proposed sensing method in Example 6. (a) Actual vectorized target-and-clutter indices $\widetilde{\boldsymbol{\xi}}$. (b) Estimated vectorized target-and-clutter indices $\widehat{\widetilde{\boldsymbol{\xi}}}$ for $r = 2$. (c) Erroneous estimated vectorized target index for $r = 2$. (d) Range-Doppler representation of the estimated target for $r = 2$, and $r = 3$.

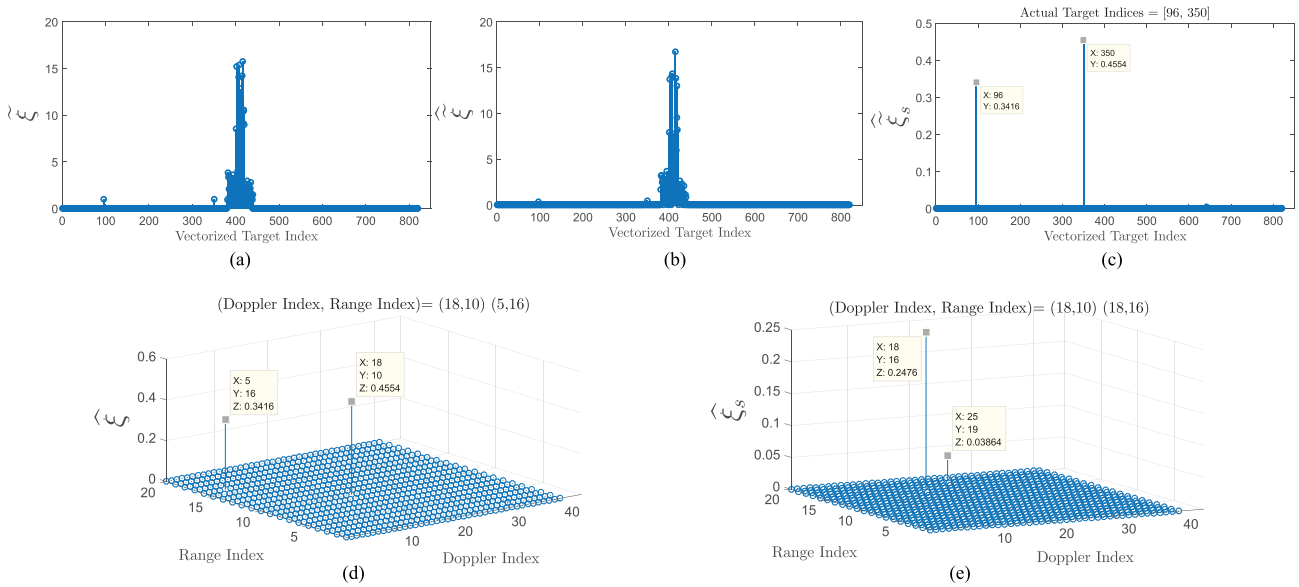

Fig. 9. Performance of the proposed sensing method in Example 7. (a) Actual vectorized target-and-clutter indices $\widetilde{\boldsymbol{\xi}}$. (b) Estimated vectorized target-and-clutter indices $\widehat{\widetilde{\boldsymbol{\xi}}}$. (c) Estimated vectorized target indices. (d) Range-Doppler representation of the estimated targets. (e) Range-Doppler representation of the estimated indices in the case of close targets.

$k_{\rm r} = 10, 16$. Indeed, this case demands for a higher sensing resolution. As it can be seen in Fig. 9(e), with $r = 3$, the proposed method has failed to identify the targets accurately. We will see in the next example that increasing the sampling rate improves sensing resolution of the proposed method. □

EXAMPLE 8 Consider the case of close targets in the previous example, i.e., with two targets located at $(k_{\rm d}, k_{\rm r}) = (18, 10)$, and $(k_{\rm d}, k_{\rm r}) = (18, 16)$ (i.e., vectorized target indices 350 and 356). This time, let the sampling rate be increased by setting $r = 4$. As it can be seen in Fig. 10, the proposed method is now able to estimate both targets accurately. □

The computational complexity of the proposed method is demonstrated by the computation time in Appendix B.

DISCUSSION 2 Let us look into the sensing parameters in the aforementioned examples, from a practical point of view. With $\omega_{\rm D} = 1600\pi$, and $K_{\rm d} = 41$, the bins for the Doppler frequency shift in our hypothetical radar are as follows:

$$f_{\rm d} = 0, \pm 40, \pm 80, \ldots, \pm 800$$

where $f_{\rm d}$ is the Doppler frequency in Hz. Suppose that the radar is working in the L-band with a carrier frequency of $f_c = 1.5$ GHz. Then, assuming a fixed (stationary) radar, according to

$$f_{\rm d} = \frac{2v}{\lambda_c}$$

the Doppler bins correspond to target velocities $v = 0, \pm 4, \pm 8, \ldots, \pm 80$ m/s, or equivalently, $v = 0, \pm 14, \ldots, \pm 280$ km/h. Based on the assumed clutter spectral distribution, the clutter is spread over the central Doppler bins, which correspond to velocities in the range $|v| \leq 4$ m/s, and according to the numerical results, the minimum detectable target speed, which is associated with the 19th (or equivalently the 23rd) Doppler bin equals to 8 m/s (i.e., 28.8 km/h or equivalently 15.5 kn). This can be a typical practical scenario in seaborne target detection, in terms of both the clutter spread, and the detectable target speeds (see Appendix C for more details). Specifically, the sea-clutter in some typical situations is confined to low target speeds of less than 4 m/s [33]. Moreover, typical seaborne targets have a speed in the range of 18 to 58 kn, which is indeed the detectable range of the proposed hypothetical scenario.[6] With $T_p = K_r \tau_0 = 0.6$ ms, the radar pulse repetition frequency (PRF) is $f_p = \frac{5}{3}$ kHz, and thus, the unambiguous range of the radar, i.e., $R_{\rm un}$ can be obtained according to $R_{\rm un} = \frac{c}{2f_p}$, where c denotes the velocity of light. This leads to an unambiguous range of 90 km for the proposed hypothetical radar. Note that this range can be simply increased by considering more range bins, i.e., by increasing K_r, which has no adverse effect on the performance of the sensing method. Therefore, assuming enough computational capacity, the unambiguous range here is not a major limitation. Finally, with $L = 41$, the coherent processing interval, at each direction, is equal to $LT_p = 24.6$ ms.

All of the above highlighted numbers and descriptions can be in agreement with the requirements of a typical seaborne target detection scenario. ■

To further evaluate the overall performance of the proposed method, we look into *the probability of perfect detection/estimation*, i.e., the probability that the number of

[6]Even slow-motion targets that move with a speed of about 16 to 18 kn would thus be detectable.

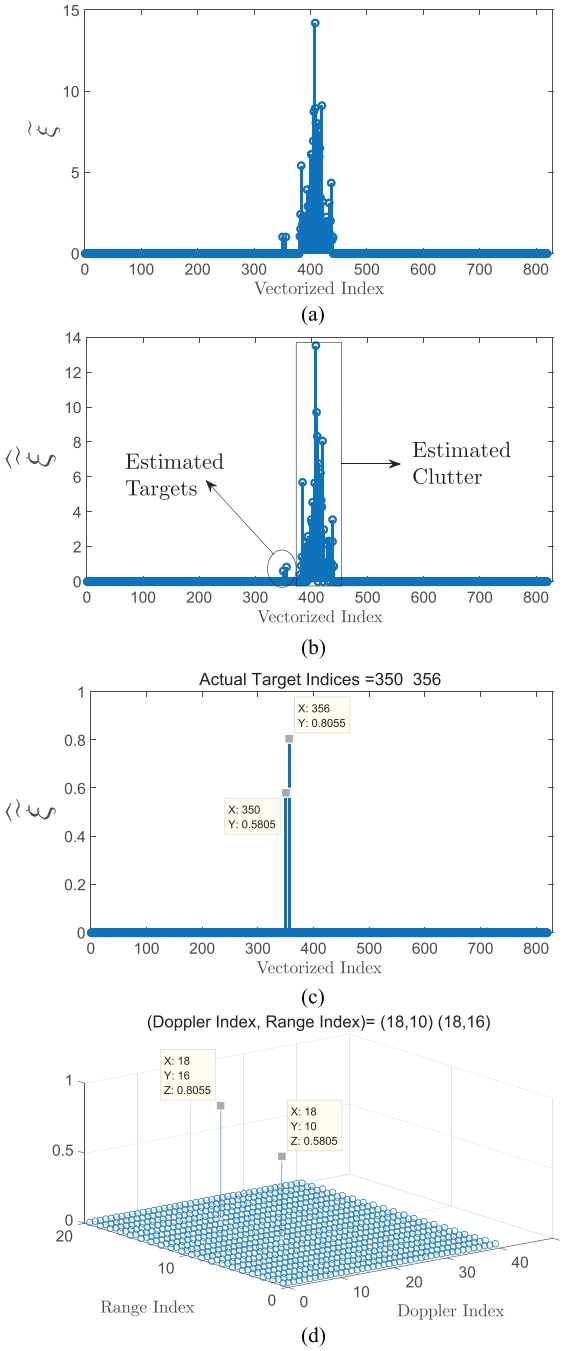

Fig. 10. Proposed sensing method for the higher target resolution scenario in Example 8. (a) Actual vectorized target-and-clutter indices $\widetilde{\boldsymbol{\xi}}$. (b) Estimated vectorized target-and-clutter indices $\widehat{\widetilde{\boldsymbol{\xi}}}$. (c) Estimated vectorized target indices. (d) Range-Doppler representation of the estimated targets.

the targets are detected correctly, and their corresponding range-Doppler indices are estimated accurately. This is in fact a metric that combines the estimation and detection performances.[7] To do so, we consider the case of a single target in the presence of the clutter considered in Fig. 5, in an SNR of 0 dB. Fig. 11 depicts the perfect detection/estimation performance of the proposed method with a sampling frequency of r/τ_0, for $r = 2, 3$, and 4 (for example, with $r = 3$, the sampling frequency is 0.1 MHz).[8] Fig. 11(a) is obtained by running 500 independent trials with random range indices at each chosen Doppler frequency. As it can be seen, increasing the sampling rate has effectively improved the performance. Fig. 11(b) shows the perfect detection/estimation performance of the proposed method over 500 independent trials, for different values of the signal-to-clutter ratio (SCR), at a fixed sampling frequency $16/\tau_0$ (i.e., with $r = 16$). As it can be seen, the performance of the method improves as the SCR increases.

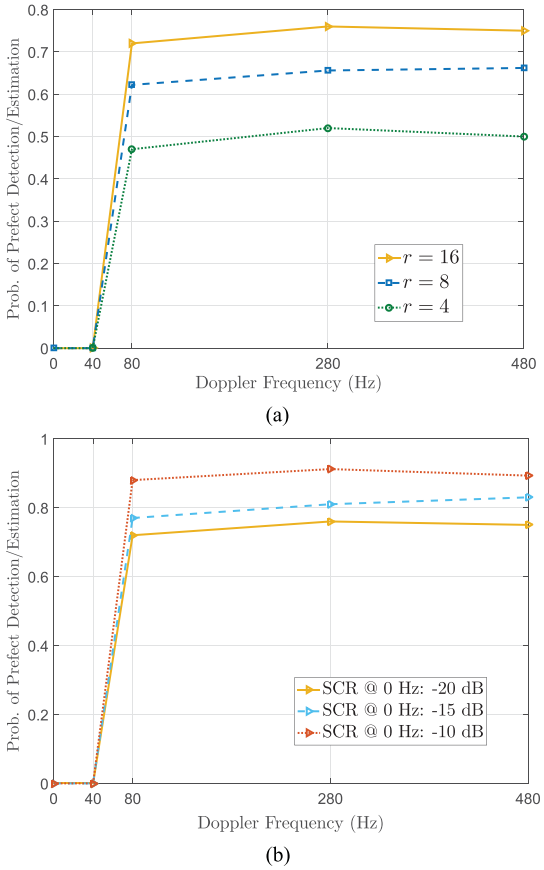

Fig. 11. Overall performance of the proposed sensing method in the presence of strong clutter. (a) SNR $= 0$ dB, and SCR$= -20$ dB (at zero Doppler frequency) for different values of r. (b) SNR $= 0$ dB, $r = 16$, for different values of SCR.

[7]Note that this metric for performance is much more strict than just the probability of detection.

[8]For a fixed (desired) value of PRF. i.e., f_p (which equivalently leads to a fixed value of the unambiguous range), the sampling frequency can be restated as $f_s = rK_{\mathrm{r}}f_p$. Therefore, technically, for any given PRF, the sampling frequency can be set within different ranges by appropriately choosing the values of r and K_r. However, increasing r and/or K_{r} increases the required computations in the proposed method. Thus, in most of the setups considered in the examples and scenarios in this paper, without loss of generality, low-to-moderate values have been considered for r and K_{r}, for computational convenience of the numerical evaluations. This is while for cases with higher values of r and K_{r}, such as those considered in Table VII and VIII in Appendix B, the sampling frequency covers a range of up to 4.8 MHz.

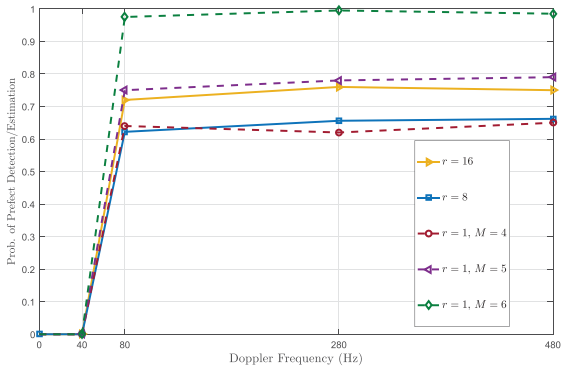

Fig. 12. Performance comparison between the proposed one-bit method and the sparse M-bit method.

Next, we will compare the performance of the proposed method, with an M-bit sparse recovery, which works as follows.

Suppose that the received signal is quantized uniformly by an M-bit quantizer. Then, similar to (40), the observed quantized signal is given by

$$\begin{cases} \mathbf{y}_{\mathrm{R}} = Q_M\left(\mathrm{Re}\left[\widetilde{\mathbf{F}}_{\mathrm{cf}}\widetilde{\boldsymbol{\xi}}_{\mathrm{cf}} + \widetilde{\mathbf{F}}_0\widetilde{\boldsymbol{\xi}}_0 + \boldsymbol{\epsilon}\right]\right) \\ \mathbf{y}_{\mathrm{I}} = Q_M\left(\mathrm{Im}\left[\widetilde{\mathbf{F}}_{\mathrm{cf}}\widetilde{\boldsymbol{\xi}}_{\mathrm{cf}} + \widetilde{\mathbf{F}}_0\widetilde{\boldsymbol{\xi}}_0 + \boldsymbol{\epsilon}\right]\right) \end{cases} \tag{40}$$

where $Q_M(\cdot)$ denotes the M-bit quantization operator. Then, with the same notations defined in the previous section, the sparse vector of the targets and the clutter can be estimated by the following unconstrained optimization problem:

$$\min_{\widetilde{\boldsymbol{\xi}}_{\mathrm{cf}},\widetilde{\boldsymbol{\xi}}_0} \left\|\mathbf{y}_{\mathrm{R}} - \mathrm{Re}\left[\tilde{\mathbf{F}}_{\mathrm{cf}}\tilde{\boldsymbol{\xi}}_{\mathrm{cf}}\right]\right\|_2 + \left\|\mathbf{y}_{\mathrm{I}} - \mathrm{Im}\left[\tilde{\mathbf{F}}_{\mathrm{cf}}\tilde{\boldsymbol{\xi}}_{\mathrm{cf}}\right]\right\|_2 + \lambda_{\mathrm{cf}}\left\|\widetilde{\boldsymbol{\xi}}_{\mathrm{cf}}\right\|_0 + \lambda_0\left\|\widetilde{\boldsymbol{\xi}}_0\right\|_0 \tag{41}$$

in which the zero-norm can be approximated by the ℓ_1-norm. Fig. 12 compares the performance of the proposed 1-bit method with that of the M-bit sparse method obtained by MATLAB's CVX toolbox according to (41).

It can be seen in Fig. 12 that the one-bit method with $r = 8$ and 16 performs almost like the sparse method with a 4 and 5 bit ADC and a Nyquist sampling ($r = 1$), respectively. Therefore, by accepting an increase in the processing bits (with respect to the sparse method that works with multibit quantized data) the proposed method provides favorable features of the one-bit method, especially the inexpensiveness of its hardware and its extremely low power consumption. We must note that the mentioned increase in the processing bits is at the software side of the receiver and is therefore not a burden in terms of hardware implementation. Moreover, the considered setup for realizing the proposed one-bit method in this paper has no optimality in terms of the setting of parameters such as λ_{cf} and λ_0, and also in terms of selecting the time-varying threshold, $h(t)$, which has significant effect on the performance. It is thus possible to further improve the performance of the proposed method and therefore reduce the processing bit overhead with respect to the optimal multibit sparse method. This invites for further study of the proposed 1-bit method from an optimal design perspective.

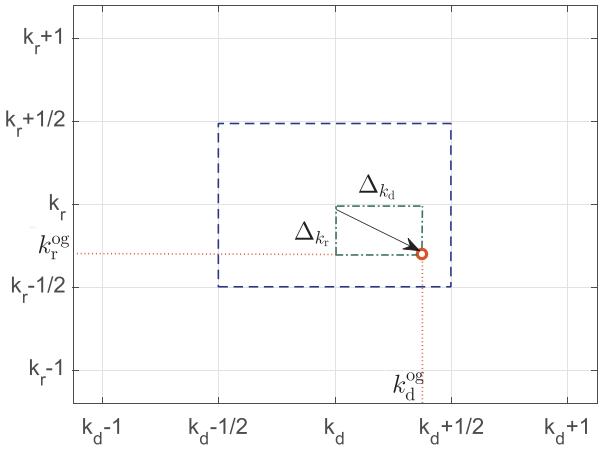

Fig. 13. Off-grid target in the range-Doppler domain.

C. Off-Grid Analysis and Clutter Doppler Resolution

In order to investigate the off-grid effect on the performance of our method, we must first update the received signal in our model for off-grid target and clutter. To begin, we consider the clutter-free scenario first, and then we add the clutter effect as well.

Consider an off-grid target with a time delay τ_{og} and the Doppler frequency of ω_{og}. Let k_{r} and k_{d} denote the closest range and Doppler indices to the off-grid target, i.e.,

$$\begin{cases} \tau_{\mathrm{og}} = k_{\mathrm{r}}\frac{\tau_0}{r} + \Delta_{\tau_{\mathrm{og}}} \\ \omega_{\mathrm{og}} = \omega_{k_{\mathrm{d}}} + \Delta_{\omega_{\mathrm{og}}} = -\omega_D + (k_{\mathrm{d}} - 1)\Delta + \Delta_{\omega_{\mathrm{og}}} \end{cases} \tag{42}$$

where $\Delta = \frac{2\omega_D}{K_{\mathrm{d}}-1}$, $|\Delta_{\tau_{\mathrm{og}}}| < \frac{\tau_0}{2}$, $|\Delta_{\omega_{\mathrm{og}}}| < \frac{\Delta}{2}$. Let

$$\begin{cases} \Delta_{k_{\mathrm{r}}} \triangleq \frac{r\Delta_{\tau_{\mathrm{og}}}}{\tau_0} \\ \Delta_{k_{\mathrm{d}}} \triangleq \frac{\Delta_{\omega_{\mathrm{og}}}}{\Delta} \end{cases}. \tag{43}$$

It is clear that $|\Delta_{k_{\mathrm{d}}}| \le \frac{1}{2}$, and $|\Delta_{k_{\mathrm{r}}}| \le \frac{1}{2}$. Replacing (43) in (42), we have

$$\begin{cases} \tau_{\mathrm{og}} = \underbrace{(k_{\mathrm{r}} + \Delta_{k_{\mathrm{r}}})}_{\triangleq k_{\mathrm{r}}^{\mathrm{og}}}\tau_0/r \\ \omega_{\mathrm{og}} = -\omega_D + \underbrace{(k_{\mathrm{d}} + \Delta_{k_{\mathrm{d}}}}_{\triangleq k_{\mathrm{d}}^{\mathrm{og}}} - 1)\Delta \end{cases} \tag{44}$$

which is illustrated in the range-Doppler domain in Fig. 13. We can now modify the received signal in our model. As for the Doppler frequency, $\boldsymbol{\phi}$ and $\boldsymbol{\Phi}$, in (23) and (24) are updated by substituting $\omega_{k_{\mathrm{d}}}$ with ω_{og}, in their k_{d}'th row, as follows:

$$\boldsymbol{\phi}_{\mathrm{og}} = \left[e^{-j\omega_D\frac{\tau_0}{r}}, \ldots, \underset{\uparrow}{e^{-j\omega_{\mathrm{og}}\frac{\tau_0}{r}}}, \ldots, e^{j\omega_D\frac{\tau_0}{r}}\right]^T \tag{45}$$

and

$$\boldsymbol{\Phi}_{\mathrm{og}} = \left[\boldsymbol{\phi}_{\mathrm{og}}\left|\boldsymbol{\phi}_{\mathrm{og}}^{(2)}\right|\cdots\left|\boldsymbol{\phi}_{\mathrm{og}}^{(M)}\right.\right]. \tag{46}$$

As for the range, the k_{r}'th column of $\mathbf{F}$ has to be modified. Having understood the required modifications for the range and Doppler off-grid, we may now check the performance of the proposed method for off-grid targets, in the following examples and simulations.

TABLE IV
Parameters in Example 9

N_t	SNR	N	r	K_r	K_d	L	τ_0	ω_D	λ
4	3 dB	8	2	40	21	5	0.01 ms	2000π rad/sec	1

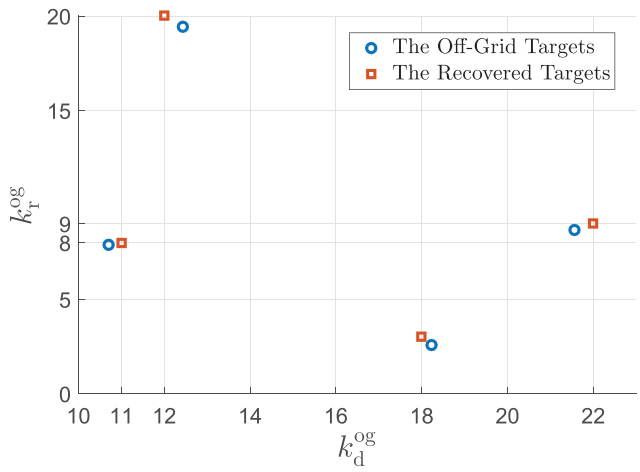

Fig. 14. Performance of the proposed method with off-grid targets in Example 9.

EXAMPLE 9 Consider the scenario with parameters set according to Table IV, in which N_t is the number of targets and the SNR is measured with respect to the weakest target. The actual off-grid range-Doppler indices $(k_\mathrm{d}^{\mathrm{og}}, k_\mathrm{r}^{\mathrm{og}})$ of the four targets in this example are $(10.6932, 7.8844)$, $(21.5524, 8.6783)$, $(12.4308, 19.4482)$, and $(18.2383, 2.6026)$. Fig. 14 shows the actual range-Doppler indices of the four off-grid targets and their on-grid recovery by the proposed method. As it can be seen, all four targets have been detected in their nearest range-Doppler grids. □

EXAMPLE 10 In order to see the overall performance of the proposed method at the presence of off-grid targets, we consider an experiment with 100 independent trials of detecting a single target with off-grid indices $k_\mathrm{r}^{\mathrm{og}}$ and $k_\mathrm{d}^{\mathrm{og}}$ uniformly distributed over $[0.5,\ k_\mathrm{r}+0.5] \in \mathbb{R}$, and $[0.5,\ k_\mathrm{d}+0.5] \in \mathbb{R}$, respectively. We look into the average index error. Specifically, consider a scenario with parameters set according to Table IV, but with $N_t = 1$. Fig. 15 shows the off-grid targets within the 100 trials in the range-Doppler domain, where the green dots show the targets, which have been detected at their nearest range-Doppler grids (i.e., optimal w.r.t. the on-grid recovery limitation), whereas the red dots show the targets, which have been detected suboptimally with either their estimated range or Doppler index being different than the nearest ones.

In this experiment, 52% of the off-grid targets have been detected optimally at the nearest range and Doppler grids. For each off-grid target, let O_r and O_d, respectively, denote the range-index offset and the Doppler-index offset defined as

$$\begin{cases} O_\mathrm{r} \triangleq \frac{|k_\mathrm{r}^{\mathrm{og}} - \widehat{k}_\mathrm{r}|}{k_\mathrm{r}^{\mathrm{og}}} \\ O_\mathrm{d} \triangleq \frac{|k_\mathrm{d}^{\mathrm{og}} - \widehat{k}_\mathrm{d}|}{k_\mathrm{d}^{\mathrm{og}}} \end{cases} \tag{47}$$

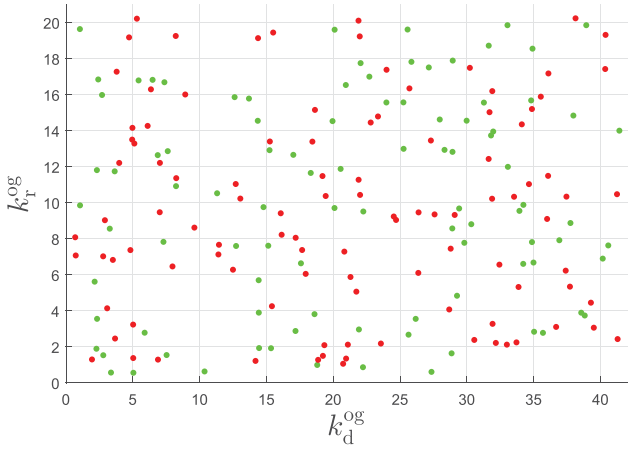

Fig. 15. Overall performance of the proposed method at the presence of off-grid targets in Example 10: Optimal and suboptimal estimation of the off-grid targets.

TABLE V
Summary of the Results for Example 10 and 11

	$r=2$	$r=3$	$r=4$
Optimal On-grid Estimation	%52	%62	%68
$\overline{O}_r$	0.0921	0.0705	0.0545
$\overline{O}_d$	0.06	0.0428	0.0376

where $\widehat{k}_\mathrm{r}$ is the on-grid estimation of $k_\mathrm{r}^{\mathrm{og}}$, and $\widehat{k}_\mathrm{d}$ is the on-grid estimation of $k_\mathrm{d}^{\mathrm{og}}$.

Now, let $\overline{O}_\mathrm{r}$ (resp. $\overline{O}_\mathrm{d}$) denote the average range-index (resp. Doppler-index) offset over the 100 independent trials in our experiment. It is seen that $\overline{O}_\mathrm{r} = 0.0920$, and $\overline{O}_\mathrm{d} = 0.06$, which shows the overall suboptimal performance of the proposed method at the presence of off-grid targets. □

EXAMPLE 11 In this example, we want to investigate the effect of increasing r at the presence of off-grid targets. Consider the same scenario and parameters of Example 10, with r increased to 3 and 4. The results show an improvement in the performance. Specifically, by increasing r to 3, the percentage of optimal target recovery is increased to 0.62, and the average range and Doppler index offsets are decreased to $\overline{O}_\mathrm{d} = 0.0428$, and $\overline{O}_\mathrm{r} = 0.0705$. Now further increasing r to 4, 0.68% of the trials have shown optimal recovery and the following results have been made: $\overline{O}_\mathrm{d} = 0.0376$ and $\overline{O}_\mathrm{r} = 0.0545$. Table V summarizes the results of Examples 10 and 11, which shows the role of r in the performance of the proposed method at the presence of off-grid targets. □

Now that we have looked into the off-grid effect in the clutter-free scenario, we move on to the case of off-grid clutter, which can be addressed in a similar fashion by similarly modifying $\boldsymbol{\phi}$ and $\boldsymbol{\Phi}$ for the Doppler index and the columns of $\mathbf{F}$ for the range index, which updates $\widetilde{\mathbf{F}}_0$ in

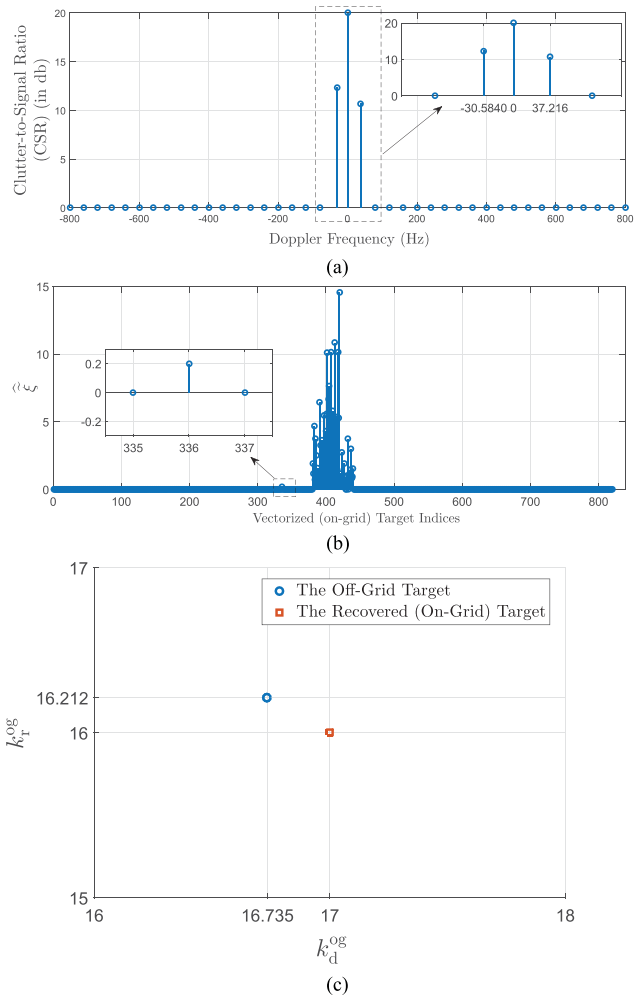

Fig. 16. Performance of the proposed method at the presence of off-grid clutter in Example 12. (a) Representation of the off-grid clutter. (b)-(c) On-grid recovery of the off-grid target at the presence of strong off-grid clutter.

the formulation of the received signal in the clutter-affected scenario.[9]

EXAMPLE 12 Consider the scenario of Example 5, i.e., the case with the parameters given in Table III. In order to include the off-grid clutter effect into this example, we suppose that the side-clutter components (the ones with nonzero Doppler frequencies) are located at two random frequencies $f_{\rm c}^-$, and $f_{\rm c}^+$ (in Hz), uniformly distributed over $[-\frac{3\Delta}{2\pi}, -\frac{\Delta}{2\pi}] = [-60, -20]$, and $[\frac{\Delta}{2\pi}, \frac{3\Delta}{2\pi}] = [20, 60]$, respectively. As for the CSR, we similarly assume that the CSR is 20 dB at the zero-Doppler frequency, and decays at a rate of 0.25 dB/Hz, confined to ± 60 Hz.[10] Fig. 16(a) shows one such realization of such off-grid clutter. Now consider an off-grid target located at $(k_d^{\rm og}, k_r^{\rm og}) = (16.7325, 16.2124)$ for example. Fig. 16(b) and (c), respectively, shows the estimated target-and-clutter, and the estimated target. As it

[9]We have assumed that within the clutter Doppler spread, the clutter exists in all the range grids. Therefore, the modifications addressing the range off-grid have to be performed over all the columns of $\mathbf{F}$.

[10]In Example 5, the on-grid clutter was confined to ± 40 Hz.

TABLE VI
Parameters in Example 13

N_t	SNR	δ	N	r	$K_{\rm r}$	$K_{\rm d}$	L	τ_0	$\omega_{\rm D}$	$\lambda_{\rm cf}$	λ_0
1	5 dB	4	8	3	20	81	81	0.03 ms	800π rad/sec	6/7	1/7

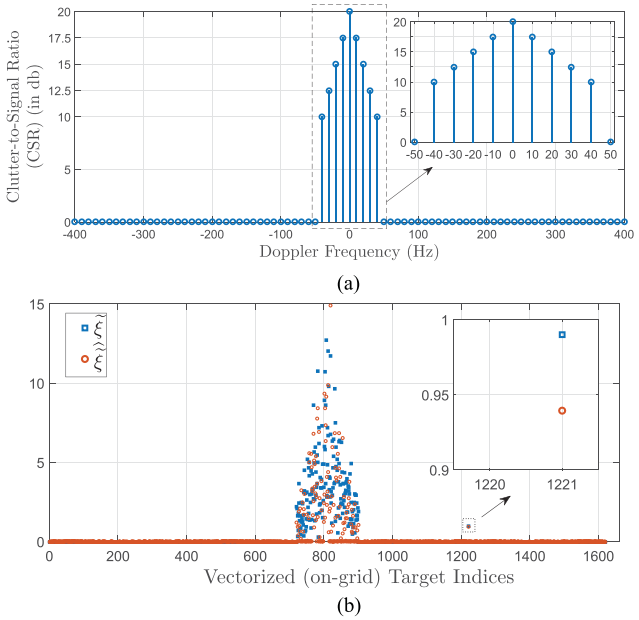

Fig. 17. Performance of the proposed method at the presence of strong clutter in Example 13. (a) Doppler spectral representation of the clutter. (b) Accurate recovery of the target.

can be seen, the proposed method has performed optimal w.r.t. the on-grid recovery limitations at the presence of the off-grid clutter shown in Fig. 16(a). □

As for the second part of this section, in the following example, we look into the resolution of the Doppler cells, and the number of Doppler cells that clutter occupies.

EXAMPLE 13 Consider a scenario with parameters set according to Table VI. With these parameters, the resolution of the Doppler frequency cells is now 10 Hz, and the clutter is assumed to be spread over $2\delta + 1 = 9$ Doppler cells. Fig. 17 shows the performance of the proposed method for a randomly located target under this setup. As it can be seen the target has been accurately identified. □

D. Note on the Realization of the Time-Varying Thresholds

Before concluding the paper, we shall further remark on the time-varying thresholds in the proposed method.

As mentioned previously, in the numerical examples and the simulations carried out in this paper, the thresholds have been modeled by independent realizations of a continuous random variable uniformly distributed over the normalized amplitude of the reflected signals. In practice, however, the quantizing threshold itself has a finite resolution, i.e., it takes values from discrete levels. The finer these levels are, the more hardware requirement we will face in the realization of $h_{\rm R}(t)$ and $h_{\rm I}(t)$ (e.g., by using a digital to analog converter). On the other hand, throughout the paper,

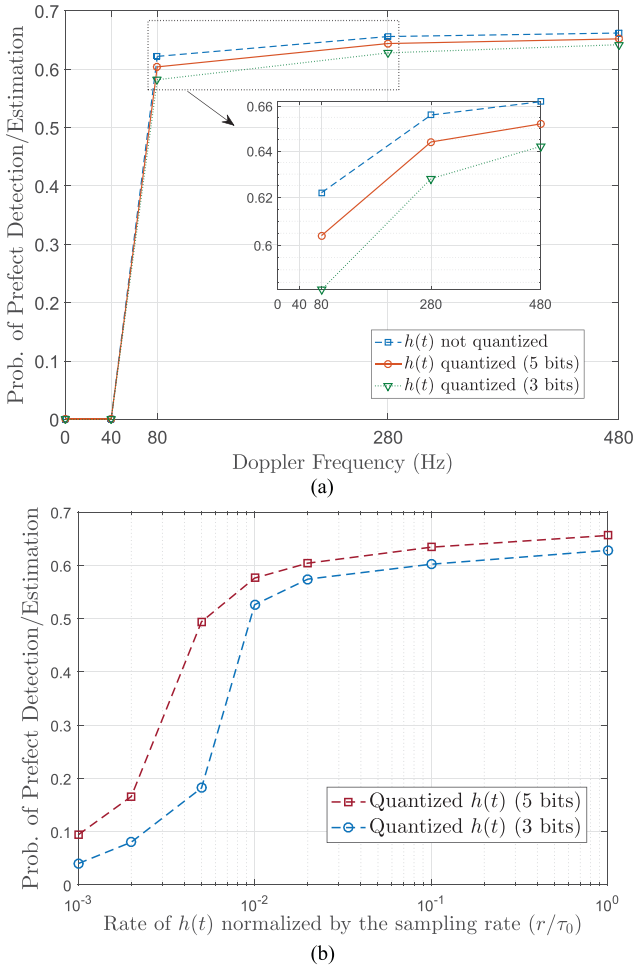

Fig. 18. (a) Comparison between the performance of the proposed one-bit method in quantized versus non-quantized thresholds for $r = 8$. (b) The performance of the proposed method with $r = 8$, at the Doppler frequency of 280 Hz, with different changing-rates for the time-varying thresholds.

the thresholds were changed sample by sample, that is with a rate of r/τ_0. This also affects the realization cost of the time-varying thresholds.

Therefore, in order to maintain the discussed advantages of the 1-bit ADC used in the proposed method, we must keep the time-varying thresholds as simple as possible, from the resolution and the changing-rate perspective.

Here, we will thus examine the performance of the proposed method for simplified threshold sequences. Specifically, we first repeat the simulation of Fig. 11(a) with $h_{\mathrm{R}}(t)$ and $h_{\mathrm{I}}(t)$ chosen from 32 and 8 uniformly spaced levels (i.e., in 5 and 3 b, respectively). As it can be seen in Fig. 18(a), the quantized realization of the thresholds does not considerably affect the performance of the proposed method, even with a low resolution of 3 bits.

Next, we will repeat the simulation by considering different changing-rates for $h(t)$ at a given Doppler frequency. Fig. 18(b) depicts the probability of perfect detection/estimation at the Doppler frequency of 280 Hz, for different changing-rates of $h(t)$. Considering the parameter setup for this simulation, and specifically, the PRF, we can see from Fig. 18(b) that instead of sample by sample, the time-varying threshold can change with a rate as low as a fraction of the PRF, without much performance degradation. This means that the thresholds can be fixed over multiple pulse repetition intervals, which can further simplify the realization of the time-varying thresholds in practice.

V. CONCLUSION

A compressive pulse-Doppler radar based on one-bit quantization of the received noisy signal was proposed. The problem was first considered in a clutter-free framework. Because of the sparsity of the targets in the range-Doppler domain, the problem was approached by a sparse recovery method, which leads to an optimization problem that could be tackled numerically. Numerical examples showed that the proposed sensing method has a promising performance in this case. It was further seen that increasing the sampling rate at the receiver can compensate for the performance loss of low SNR. This feature makes the proposed method even more favorable, knowing that one-bit quantization allows for high sampling rates at a low cost. The performance of the proposed method was then further evaluated in terms of the dynamic range of the targets. It was seen that in the case of high dynamic range, by increasing the sampling rate, the method is able to estimate the targets accurately with a high probability. The problem was then further considered in a clutter-affected framework. It was shown how the proposed method can be modified to work in the presence of strong clutter. Various numerical examples and simulation results were then provided to evaluate the performance of the proposed method. It was seen that the proposed method has good sensing performance even when strong clutter is around. It was further observed that increasing the sampling rate at the receiver compensates for the performance loss caused by strong clutter. The performance of the proposed method was further compared to a multibit sparse method. The comparison suggests that the favorable hardware features of the proposed method, such as low power consumption and inexpensiveness, comes only at the price of possibly increasing the processing bits at the software side. It was further seen that the method performs well at the presence of off-grid target and clutter. Finally, it was seen that the realization of the time-varying thresholds can be simplified by choosing the thresholds from a small number of discrete levels, and by changing the thresholds as slowly as possible.

APPENDIX A

Proof of Lemma 1: Considering the formula for the received signal in (3), for a given $(k_{\mathrm{r}}, k_{\mathrm{d}})$, we focus on

$$\sum_{\ell,n} c_n p(t - n\tau_0 - \ell T_p - \tau_{k_{\mathrm{r}}}) e^{j\omega_{k_{\mathrm{d}}} t}. \tag{48}$$

Knowing that $p(t)$ is nonzero only for $0 \le t < \tau_0$, in order to identify the nonzero elements of $\mathbf{F}$, we must consider the following constraint:

$$0 \le t - n\tau_0 - \ell T_p - \tau_{k_{\mathrm{r}}} < \tau_0 \tag{49}$$

TABLE VII
Elapsed Time (in seconds) for the Clutter-Free Scenario

ELAPSED TIME VERSUS $K_{\rm d}$ FOR $K_{\rm r}=20$, $r=4$, $L=8$

	$k_{\rm d}=41$	$k_{\rm d}=61$	$k_{\rm d}=81$	$k_{\rm d}=101$	$k_{\rm d}=121$	$k_{\rm d}=141$	$k_{\rm d}=161$	$k_{\rm d}=181$
Traditional Pulse-Doppler ($N=4$)	0.0536	0.0761	0.0908	0.1120	0.1359	0.1617	0.1783	0.1952
The Proposed Method ($N=4$)	0.8389	0.9565	1.1604	1.3965	1.6999	1.8880	2.2027	2.5031
The Proposed Method ($N=8$)	1.2162	1.7433	2.3483	2.8249	3.3115	3.7802	4.2725	4.9264

ELAPSED TIME VERSUS $K_{\rm r}$ FOR $K_{\rm d}=41$, $r=4$, $L=8$

	$k_{\rm r}=20$	$k_{\rm r}=40$	$k_{\rm r}=60$	$k_{\rm r}=80$	$k_{\rm r}=100$	$k_{\rm r}=120$	$k_{\rm r}=140$	$k_{\rm r}=160$
Traditional Pulse-Doppler ($N=4$)	0.0536	0.0970	0.1448	0.1979	0.2387	0.2908	0.3508	0.3839
The Proposed Method ($N=4$)	0.8389	1.3210	2.2112	3.1453	4.1809	5.2236	6.6199	8.3731
The Proposed Method ($N=8$)	1.2162	2.3674	3.5718	5.0899	6.6610	8.2925	10.2732	12.3813

ELAPSED TIME VERSUS r FOR $K_{\rm r}=20$, $K_{\rm d}=41$, $L=8$

	$r=2$	$r=4$	$r=6$	$r=8$	$r=10$	$r=12$	$r=14$	$r=16$
$N=4$	0.5852	0.6938	0.9519	1.2577	1.5367	1.8816	2.2058	2.7701
$N=8$	0.6583	1.1784	1.7836	2.6675	3.2676	4.0866	4.9850	6.4309

ELAPSED TIME VERSUS L FOR $K_{\rm r}=20$, $K_{\rm d}=41$, $r=4$

	$L=8$	$L=10$	$L=12$	$L=14$	$L=16$	$L=18$	$L=20$
$N=4$	0.8733	0.8683	1.0673	1.3318	1.4649	1.5371	1.7431
$N=8$	1.2505	1.5491	1.9590	2.3259	2.8480	3.1619	3.8642

where $t=m\tau_0/r$, for $m=1,\ldots,M$, and $T_p=K_r\tau_0$. Starting with $\ell=0$, the above constraint thus leads to

$$0\le m-rn-k_{\rm r}<r \tag{50}$$

which can be equivalently stated as follows:

$$rn\le m-k_{\rm r}<r+rn. \tag{51}$$

Knowing that m and k are integers, the above constraint expands as the union of the following set of r equality constraints:

$$\begin{aligned} m-k_{\rm r}&=rn\\ m-k_{\rm r}&=rn+1\\ &\vdots\\ m-k_{\rm r}&=rn+r-1 \end{aligned} \tag{52}$$

which serve as the connection between the rows and columns of $\mathbf{F}$ for $m\le rK_{\rm r}$ (the range of rows corresponding to $\ell=0$). The equations in (52) are the reason behind the r repetitions of c_n (denoted by $\mathbf{c}_n$), in r consecutive rows of $\mathbf{F}$.

The rows with $m>rK_{\rm r}$ are related to $\ell=1,\ldots,L-1$. Assuming that $K_{\rm r}>N$ (which usually holds in practice), for $\ell=1$, (52) is modified as follows:

$$\begin{aligned} (m-rK_{\rm r})-k_{\rm r}&=rn\\ (m-rK_{\rm r})-k_{\rm r}&=rn+1\\ &\vdots\\ (m-rK_{\rm r})-k_{\rm r}&=rn+r-1 \end{aligned} \tag{53}$$

which governs the next $rK_{\rm r}$ rows, i.e., for $rK_{\rm r}+1\le m<2K_{\rm r}$. Comparing (52) and (53), it is clear that (53) is simply a shifted version of (52) with respect to m and thus, in every column, the second $rK_{\rm r}$ entries are repetitions of the first $rK_{\rm r}$ entries. It is not hard to check that this is also the case for $\ell=2,\ldots,L-1$, with the following set of inequalities:

$$\begin{aligned} (m-r\ell K_{\rm r})-k_{\rm r}&=rn\\ (m-r\ell K_{\rm r})-k_{\rm r}&=rn+1\\ &\vdots \qquad\qquad \ell=2,\ldots,L-1\\ (m-r\ell K_{\rm r})-k_{\rm r}&=rn+r-1 \end{aligned} \tag{54}$$

which correspond to the remaining rows of $\mathbf{F}$. Consider the set of all equations given in (52), (53), and (54), i.e.,

$$\begin{aligned} (m-r\ell K_{\rm r})-k_{\rm r}=rn+x,\quad & x=0,1,\ldots,r\\ & \ell=0,1,\ldots,L-1. \end{aligned} \tag{55}$$

The proof is then straightforward by showing that for any given values of m and $k_{\rm r}(>N)$, only one of the rL equations in (55) may be satisfied at most. ■

APPENDIX B

Regarding the computational complexity of the proposed sensing, method, here we provide various time-tables (Tables VII and VIII) that summarize the Elapsed time for running the proposed method via MATLAB on a 2.6 GHz Core i7-6700HQ CPU. For each instance, the elapsed time has been averaged over 100 similar independent trials. In the first two subtables, the elapsed time has been put in perspective with that of the traditional pulse-Doppler radar. Specifically, we look into a lower approximate for the computation time of the traditional pulse-Doppler radar, by considering its total required fast Fourier transforms (FFT). This includes the FFTs in the implementation of the matched-filter for the range compression [33], [39], and an FFT of size

TABLE VIII
Elapsed Time (in seconds) for the Clutter-Affected Scenario

ELAPSED TIME VERSUS r FOR $K_{\rm r} = 20$, $K_{\rm d} = 41$, $L = 41$.

	$r = 2$	$r = 4$	$r = 6$	$r = 8$	$r = 10$	$r = 12$	$r = 14$	$r = 16$
$N = 4$	2.9960	7.2491	12.8243	14.4896	16.9754	19.9747	22.5125	25.4942
$N = 8$	6.9845	13.4414	18.7890	24.5700	30.4385	41.3821	49.4363	58.2794

ELAPSED TIME VERSUS $K_{\rm r}$ FOR $r = 4$, $K_{\rm d} = 41$, $L = 41$.

	$k_{\rm r} = 20$	$k_{\rm r} = 30$	$k_{\rm r} = 40$	$k_{\rm r} = 50$	$k_{\rm r} = 60$	$k_{\rm r} = 70$	$k_{\rm r} = 80$
$N = 4$	3.1978	4.3377	6.0173	7.7461	9.1840	11.0370	12.8206
$N = 8$	7.3946	12.4923	17.17434	21.0551	24.0865	29.3307	33.2571

ELAPSED TIME VERSUS $K_{\rm d}$ FOR $K_{\rm r} = 20$, $r = 4$ ($L = K_{\rm d}$)

	$k_{\rm d} = 41$	$k_{\rm d} = 61$	$k_{\rm d} = 81$	$k_{\rm d} = 101$	$k_{\rm d} = 121$
$N = 4$	3.4388	7.1641	14.4730	25.1908	36.4842
$N = 8$	7.3502	19.6229	40.1073	72.2829	108.4520

TABLE IX
The Average Wind Speed in Eleven States of the US

State	Wind Speed (km/h)
Houston, Texas	12.2
Miami, Florida	14.8
Portland, Oregon	12.7
San Diego, California	11.3
New Orleans, Louisiana	13.2
Milwaukee, Wisconsin	18.5
Chicago, Illinois	16.6
Detroit, Michigan	16.4
Buffalo, New York	19
Boston, Massachusetts	19.8
Baltimore, Maryland	14

$2L$ (per range bin) for Doppler processing.[11] To interpret this comparison in a fair manner, we must note that the FFT considered in the traditional method is an efficient implementation of the discrete Fourier transform. This is while the numerical studies carried out for the proposed method in this paper, utilize the CVX optimization toolbox in its default settings, which is not necessarily computationally efficient. Indeed, one may be able to alter the CVX algorithmic settings in a way that reduces the computational time, without affecting the optimization performance by much, or may replace the CVX algorithms with a more efficient method. Moreover, the main incentive behind the studied approach was to reduce the hardware cost and energy consumption, rather than the computational cost. We believe that the goal has been achieved at the price of a computational cost, which is tolerable, especially now that cloud-computation has become more promising for radar processing such as those in vehicular technologies.

APPENDIX C

In Table IX, the average wind speed is given in 11 states in the US, which have a coastline.

[11] The requirement for FFTs of size $2L$ in Doppler processing in the traditional method are imposed by the effects of Straddle loss [39]. Moreover, the choice of L has to take into account the Doppler cell resolution of our proposed method which depends on $K_{\rm d}$.

TABLE X
Relevance Between the Wind Speed and the Sea Waves

Wind Speed (km/h)	Sea Wave Speed (ft/sec)
≤ 19	≤ 9.3
≤ 37	≤ 19.5
≤ 56	≤ 29.2

The major source of sea clutter are the waves whose speed depends very much on the wind speed. In Table X, typical ranges of the sea wave speed is given based on their relevant wind speed.

Having such typical information, one can grasp *a priori* knowledge of the maximum clutter spread. If we model the wind speed as a random variable, knowing the average would result in designs that work well on average. However, depending on how critical the application is, one may be interested in the worst case (least favorable) scenarios. In such cases, the maximum measured wind speed can be the design reference.

REFERENCES

[1] B. Le, T. Rondeau, J. Reed, and C. Bostian
Analog-to-digital converters
IEEE Signal Process. Mag., vol. 22, no. 6, pp. 69–77, Nov. 2005.

[2] B. Murmann
ADC performance survey 1997-2013
Jul. 2018. [Online]. Available: http://www.stanford.edu∼murmann/adcsurvey.html, Accessed on: Sep. 2018.

[3] [Online] Available: www.ti.com, Accessed on: Jul. 2018.

[4] J. Mo and R. W. Heath Jr.
Capacity Analysis of MIMO Systems with One-Bit Quantization
IEEE Trans. Signal Process., vol. 63, no. 20, pp. 5498–5512, Oct. 2015.

[5] A. Host-Madsen and P. Handel
Effects of sampling and quantization on single-tone frequency estimation
IEEE Trans. Signal Process., vol. 48, no. 3, pp. 650–662, Mar. 2000.

[6] A. Ribeiro and G. B. Giannakis
Bandwidth-constrained distributed estimation for wireless sensor networks - Part II: Unknown probability density function
IEEE Trans. Signal Process., vol. 54, no. 7, pp. 2784–2796, Jul. 2006.

[7] G. Zeitler, G. Kramer, and A. Singer
Bayesian parameter estimation using single-bit dithered quantization
IEEE Trans. Signal Process., vol. 60, no. 6, pp. 2713–2726, Jun. 2012.

[8] O. Dabeer and A. Karnik
Signal parameter estimation using 1-bit dithered quantization
IEEE Trans. Inf. Theory, vol. 52, no. 12, pp. 5389–5405, Dec. 2006.

[9] O. Dabeer and E. Masry
Multivariate signal parameter estimation under dependent noise from 1-bit dithered quantized data
IEEE Trans. Inf. Theory, vol. 54, no. 4, pp. 1637–1654, Apr. 2008.

[10] E. Masry
The reconstruction of analog signals from the sign of their noisy samples
IEEE Trans. Inf. Theory, vol. 27, no. 6, pp. 735–745, Nov. 1981.

[11] Z. Cvetkovic, I. Daubechies, and B. F. Logan
Single-bit oversampled A/D conversion with exponential accuracy in the bit rate
IEEE Trans. Inf. Theory, vol. 53, no. 11, pp. 3979–3989, Nov. 2007.

[12] G. Alberti. G. Franceschetti, V. Pascazio, and G. Schirinzi
Time-domain convolution of one-bit coded radar signals
IEE Proc. F–Radar Signal Process., vol. 138, pp. 438–444, 1991.

[13] G. Franceschetti, V. Pascazio, and G. Schirinzi
Processing of signum coded SAR signal: Theory and experiments
IEE Proc. F -Radar Signal Process., vol. 138, pp. 192–198, 1991.

[14] O. Bar-Shalom and A. J. Weiss
DOA estimation using one-bit quantized measurements
IEEE Trans. Aerosp. Electron. Syst., vol. 38, no. 3, pp. 868–884, Jul. 2002.

[15] P. T. Boufounos and R. G. Baraniuk
1-bit compressive sampling
In *Proc. 42nd Annu. Conf. Inform. Sci. Syst.*, Princeton, NJ, USA, 2008, pp. 16–21.

[16] A. Zymnis, S. Boyd, and E. Candes
Compressed sensing with quantized measurements
IEEE Signal Process. Lett., vol. 17, no. 2, pp. 149–152, Feb. 2009.

[17] Y. Plan and R. Vershynin
One-bit compressed sensing by linear programming
Commun. Pure Appl. Math., vol. 66, pp. 1275–1297, 2013.

[18] L. Jacques, J. N. Laska, P. T. Boufounos, and R. G. Baraniuk
Robust 1-bit compressive sensing via binary stable embeddings of sparse vectors
IEEE Trans. Inf. Theory, vol. 59, no. 4, pp. 2082–2102, Apr. 2013.

[19] X. Dong and Y. Zhang
A MAP approach for 1-bit compressive sensing in synthetic aperture radar imaging
IEEE Geosci. Remote Sens. Lett., vol. 12, no. 4, pp. 1237–1241, Jun. 2015.

[20] Y. Plan and R. Vershynin
Robust 1-bit compressed sensing and sparse logistic regression: A convex programming approach
IEEE Trans. Inf. Theory, vol. 59, no. 1, pp. 482–494, Jan. 2013.

[21] M. Yan, Y. Yang, and S. Osher
Robust 1-bit compressive sensing using adaptive outlier pursuit
IEEE Trans. Signal Process., vol. 60, no. 7, pp. 3868–3875, Apr. 2012.

[22] U. S. Kamilov, A. Bourquard, A. Amini, and M. Unser
One-bit measurements with adaptive thresholds
IEEE Signal Process. Lett., vol. 19, no. 10, pp. 607–610, Oct. 2012.

[23] A. Ai, A. Lapanowski, Y. Plan, and R. Vershynin
One-bit compressed sensing with non-Gaussian measurements
Linear Algebra Its Appl., vol. 441, pp. 222–239, Jan. 2014.

[24] L. Zhang, J. Yi, and R. Jin
Efficient algorithms for robust one-bit compressive sensing
In *Proc. 31st Int. Conf. Mach. Learning*, Beijing, China, Jun. 2014, pp. 820–828.

[25] K. Knudson, R. Saab, and R. Ward
One-bit compressive sensing with norm estimation
IEEE Trans. Inf. Theory, vol. 26, no. 5, pp. 2748–2758, 2016.

[26] C. D. Gianelli, L. Xu, J. Li, and P. Stoica
One-bit compressive sampling with time-varying thresholds for sparse parameter estimation
In *Proc. IEEE Sensor Array Multichannel Signal Process. Workshop*, Jul. 2016, pp. 1–5.

[27] C. D. Gianelli, L. Xu, J. Li, and P. Stoica
One-bit compressive sampling via time-varying thresholds: The Cramer-Rao bound, maximum likelihood, and sparse estimation
In *Proc. 50th Asilomar Conf. Signals, Syst. Comput.*, Pacific Grove, CA, USA, Nov. 2016.

[28] J. Li, M. M. Naghsh, S. J. Zahabi, and M. Modarres-Hashemi
Compressive radar sensing via one-bit sampling with time-varying thresholds
In *Proc. 50th Asilomar Conf. Signals, Syst. Comput.*, Pacific Grove, CA, USA, Nov. 2016.

[29] S. J. Zahabi, M. M. Naghsh, M. Modarres-Hashemi, and J. Li
Compressive pulse-doppler radar sensing via 1-bit samplin with time-varying threshold
In *Proc. IEEE Int. Conf. Acoust., Speech Signal Process.*, New Orleans, LA, USA, Mar. 2017, pp. 3419–3423.

[30] R. M. Gray
Oversampled sigmadelta modulation
IEEE Trans. Commun., vol. COM-35, no. 5, pp. 481–489, May 1987.

[31] S. Hoyos, B. M. Sadler, and G. R. Arce
Monobit digital receivers for ultrawideband communications
IEEE Trans. Wireless Commun., vol. 4, no. 4, pp. 1337–1344, Jul. 2005.

[32] V. Pascazio, and G. Schirinzi
Signum coded synthetic aperture radar: The effect of oversampling on image quality
In *Proc. Int. Conf. Image Process.*, 1997, pp. 849–852.

[33] M. Skolnik
Introduction to Radar Systems, 2nd ed. New York, NY, USA: McGraw-Hill, 1980.

[34] M. S. Bazaraa and C. M. Shetty
Nonlinear Programming Theory and Algorithms. New York, NY, USA: Wiley, 1979.

[35] A. Bastounis and A. C. Hansen
On the absence of the RIP in realworld applications of compressed sensing and the RIP in levels 2014.
[Online]. Available: http://arxiv.org/abs/1411.4449

[36] A. Bastounis and A. C. Hansen
On the absence of uniform recovery in many real-world applications of compressed sensing and the RIP & nullspace property in levels
SIAM J. Imag. Sci., vol. 10, no. 1, pp. 335–371, 2017.

[37] P. Stoica, H. He, and J. Li
New algorithms for designing unimodular sequences with good correlation properties
IEEE Trans. Signal Process., vol. 57, no. 4, pp. 1415–1425, Apr. 2009.

[38] M. Grant and S. Boyd
CVX: Matlab software for disciplined convex programming (web page and software),
2014. [Online]. Available: http://stanford.edu/∼boyd/cvx

[39] M. A. Richards, J. A. Scheer, and W. A. Holm
Principles of Modern Radar Volume I-Basic Principles. Stevenage, U.K.: Scitech Publishing, 2010.

Sayed Jalal Zahabi (S'08–M'16) received the B.Sc., M.Sc., and Ph.D. degrees in electrical engineering from Isfahan University of Technology (IUT), Isfahan, Iran, Yazd University, Yazd, Iran, and IUT, in 2007, 2010, and 2015, respectively.

Since September 2016, he has been a Postdoctoral Researcher with the Department of Electrical and Computer Engineering, IUT. He has been serving as an Invited Lecturer with the Computer and IT Group and the Biomedical Engineering Group, IUT, since February 2016 and September 2017, respectively. His research interest broadly includes statistical signal processing, information theory, data compression, machine learning, and bioinformatics.

Dr. Zahabi was the recipient of the 2016 Best Ph.D. Thesis Award at Isfahan University of Technology.

Mohammad Mahdi Naghsh (S'09–M'14) received the B.Sc., the M.Sc., and the Ph.D. degrees all in electrical engineering from Isfahan University of Technology, Isfahan, Iran, in 2005, 2008, and 2013, respectively.

From May 2012 to May 2013, he was a visiting Researcher with the Department of Information Technology, Uppsala University, Uppsala, Sweden, where he was working with Prof. P. Stoica. He is currently an Assistant Professor with the Department of Electrical and Computer Engineering and also the Director of Technology Transfer Office, Isfahan University of Technology, Isfahan, Iran. He has been funded as Visiting Researcher/Professor in several universities in Italy, Sweden, and China. His research interests include applications of statistical signal processing as well as optimization techniques to active sensing/communication systems and learning.

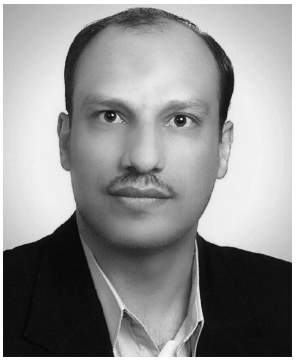

Mahmoud Modarres-Hashemi received the B.S. and M.S. degrees in 1990 and 1992, respectively, both in electrical engineering from Isfahan University of Technology (IUT), Isfahan, Iran. He received the Ph.D. degree from Sharif University of Technology, Tehran, Iran in 2000.

He is a Professor of electrical engineering with IUT. He has been the Faculty Member of the Electrical Engineering Department, IUT, since 1993 and is currently the President of IUT. His main research interests include statistical signal processing, radar signal processing, and electronic warfare.

Jian Li (F'05), photograph and biography not available at time of publication.